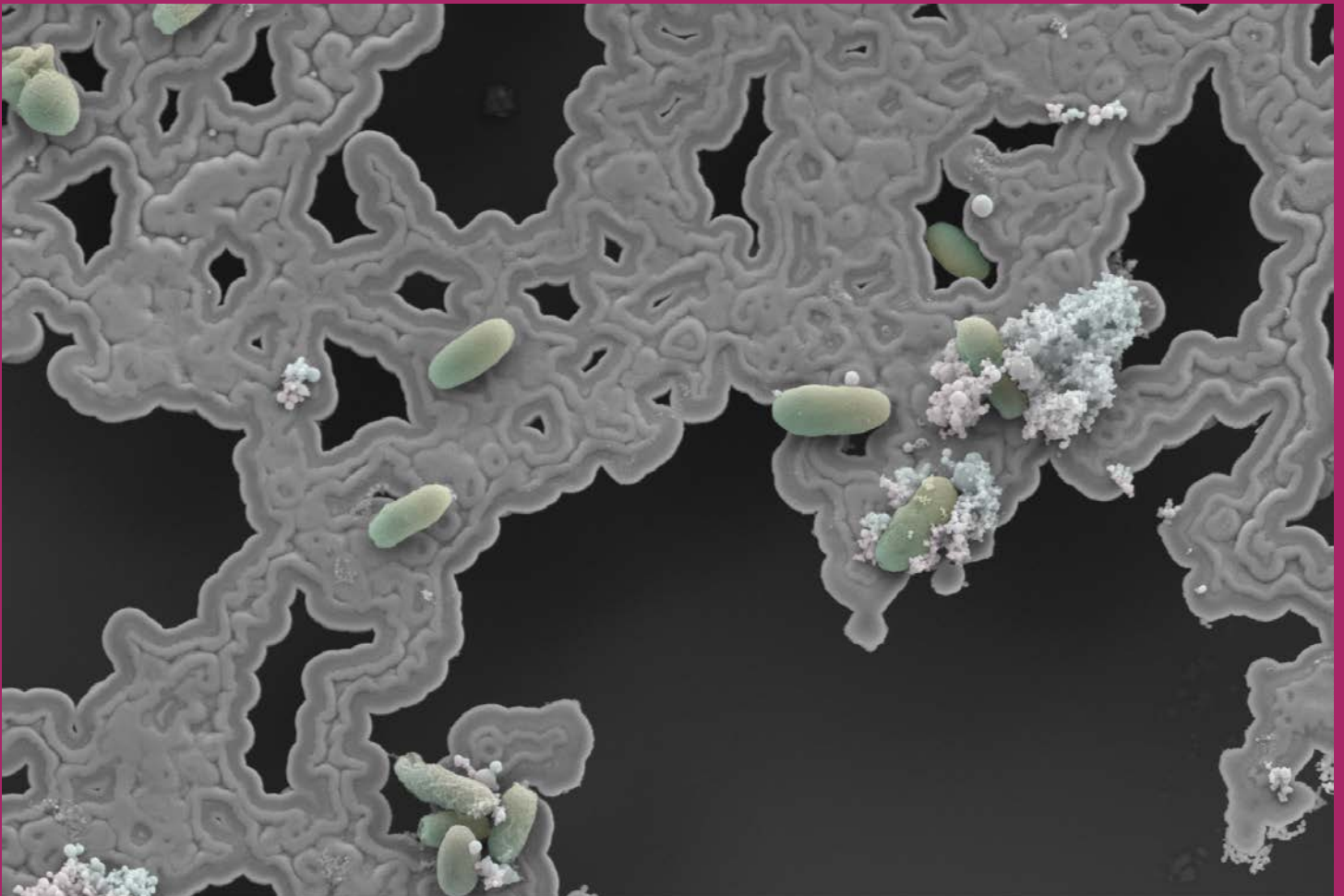




# *Texas Journal of Microscopy*



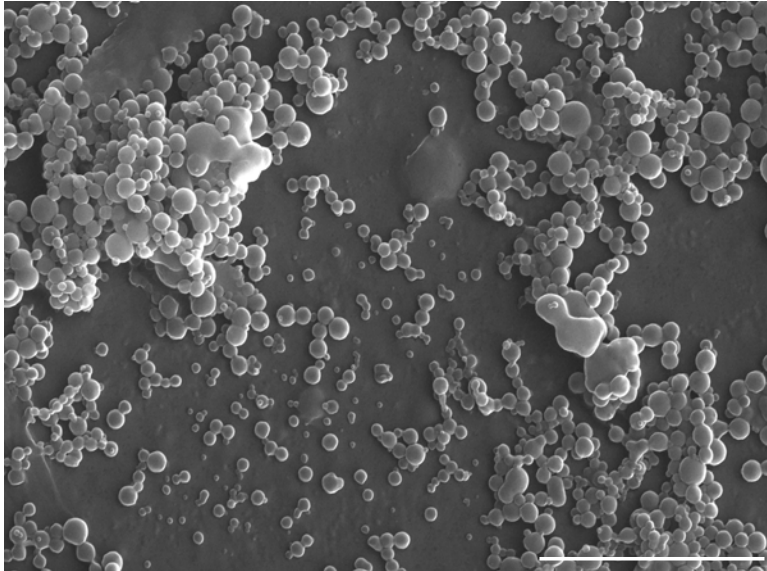
Volume 55

Number 1, 2024

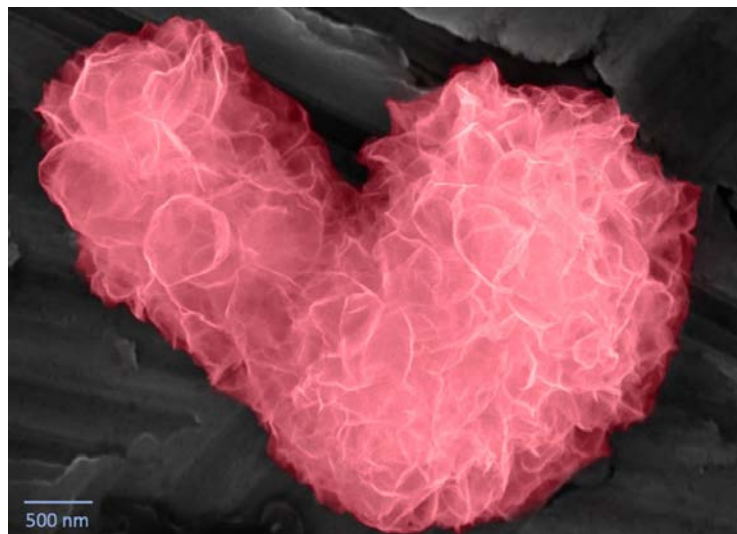
ISSN 1554-0820

Visit our website at [www.texasmicroscopy.org](http://www.texasmicroscopy.org)

# Photo Gallery



Nanoliposomes which were synthesized as carriers of an active pharmaceutical ingredient targeting the citrus greening disease. The image was acquired by Focus Ion Beam Scanning Electron Microscopy under high vacuum, at 30 kV, and 15,000x magnification. Liposomes are lipid-based spherical vesicles that self-assemble in one or more layers and can act as nanocarriers of therapeutics, such as nanoparticles, siRNA, or proteins. These drug delivery systems can be synthesized in micro or nano size and are often decorated with molecules such as antibodies or receptors to improve their drug delivery ability, therefore enhancing the therapeutic index. Courtesy of Dr. Amanda K. Sevcik, Associate Research Scientist, Sayes Research Group, Department of Environmental Science, Baylor University, Waco, TX.



A colorized scanning electron micrograph of a heart-shaped carbon nanofiber circular cluster with nanosheets of aluminum substitute nickel hydroxide grown onto them. The micrograph was obtained by Samuel W. Kimmel, PhD candidate in the Material Science, Engineering, and Commercialization Program at Texas State University.

## TSM OFFICERS 2023-2024

### President:

JOSEFINA ARELLANO-JIMENEZ  
MSE Core Characterization Facility  
The University of Texas at Dallas | Richardson, TX, 75080  
(972) 883-5759  
Josefina.Arellano@utdallas.edu

### President-elect:

VACANT

### Past President:

AMY JO HAMMETT  
Department of Biological Sciences  
The University of Texas at Dallas | Richardson, TX, 75080  
AmyJo.Hammett@UTDallas.edu

### Secretary:

AMY JO HAMMETT  
Department of Biological Sciences  
The University of Texas at Dallas | Richardson, TX, 75080  
AmyJo.Hammett@UTDallas.edu

### Secretary-elect:

VACANT

### Treasurer:

BERND ZECHMANN  
Center for Microscopy and Imaging  
Baylor University | Waco, TX 76798-7046  
(254) 710-2322  
Bernd\_Zechmann@baylor.edu

### Treasurer-elect:

VACANT

### Program Chairman:

JOYCE ANDERSON  
Shared Research Operations  
Texas State University | San Marcos, TX 78666  
(512) 245-1839  
jha39@txstate.edu

### Program Chairperson-elect:

VACANT

## APPOINTED OFFICERS

### Corporate Member Representative:

JAMES C. LONG  
Ted Pella, Inc.  
P.O. Box 492477 | Redding, CA 96049  
(530) 227-8329  
james\_long@tedpella.com

### Facebook Master:

NABARUN GHOSH  
Dept. of Life, Earth, and Environmental Sciences  
West Texas A&M University | Canyon, Texas 79015  
Phone (806) 651-2571 FAX (806) 651-2928  
nghosh@wtamu.edu

### Student Representative:

LYANNA DELEON  
Department of Life, Earth, and Environmental Sciences  
West Texas A&M University | Canyon, Texas 79015  
(806) 341-4771  
ldeleon1@buffs.wtamu.edu

### Journal Editors:

CATALINA C. PISLARIU  
Division of Biology, School of the Sciences  
Texas Woman's University | Denton, TX 76204-5799  
(940) 898-4611  
cpislariu@twu.edu

### Webmaster:

BERND ZECHMANN  
Center for Microscopy and Imaging  
Baylor University | Waco, TX 76798-7046  
(254) 710-2322  
Bernd\_Zechmann@baylor.edu

# Contents

TEXAS JOURNAL OF MICROSCOPY  
VOLUME 55, NUMBER 1, 2024  
ISSN 1554-0820



### Editor

Catalina Iulia Pislariu, PhD  
Associate Professor  
Division of Biology, School of the Sciences,  
Texas Woman's University, Denton, TX 76204

### Official Journal of the Texas Society for Microscopy

"TSM - Embracing all forms of Microscopy"

[www.texasmicroscopy.org](http://www.texasmicroscopy.org)

President's Message .....	4
Keynote Speakers for the 58th TSM Meeting .....	5
Spring 2024 Life Sciences Abstracts .....	7
Spring 2024 Material Sciences Abstracts .....	14
Spring 2024 Technical Abstracts .....	35
Corporate Members .....	41
Advertiser's Index:	
JEOL .....	44

### ON THE COVER

The cover image shows a scanning electron micrograph of bacteria and associated matrix fixed directly from Petri plate surface and post stained with OTO methods, mounted on mica, sputter coated, and imaged with ET detector at 5kV. The specimen is a symbiont isolated from an insect host.

Courtesy of the Moran Lab at the University of Texas at Austin. Image captured by Michelle Mikesh, Electron Microscopy Specialist at the Center for Biomedical Research, UT Austin

---

---

# President's Message

---

**I**t is a special time when all the members of the Texas Society for Microscopy get together as a community. Almost one year has passed since we meet for the 57th annual meeting in Dallas-Richardson in 2023. We had the opportunity to learn about in-situ TEM, Focused Ion Beam Microscopy, and E-beam lithography during the workshops organized at the Natural Science and Engineering Research Laboratory at UT Dallas, sponsored by Protochips, Thermo Fisher, and Raith on Thursday. It was great to meet over dinner that evening to reconnect with old friends and get to know new members. Then, attending to the full-day program on Friday with amazing lectures from our keynote speakers Daniela Nicastro from UT Southwestern Medical Center, Alice Liang from New York University Grossman School of Medicine, and Moon Kim from UT Dallas, and excellent 15 platform presentations. Congratulations to all the eight students who participated in the student competition! Also, congratulations to all the students participating in the poster session! One of the core missions of TSM is supporting students. In 2023 we granted traveling support to 20 students to attend the meeting in Dallas-Richardson and we announced the winner of the Small Grant Program 2023, Christian Landry from Texas A&M University.

This year, Joyce Anderson has done an amazing job organizing the 58th annual meeting in San Marcos. We want to thank Evident (formerly Olympus), Horiba, and Thermo Fisher, for sponsoring the workshops at the Shared Research Operations Facility, at Texas State University and for showing us the latest advances in the field of Confocal Laser Scanning Microscopy, Tip-Enhanced Raman Spectroscopy, and XPS and STEM-EDS. We are very proud to support and display the hard work of our members. We look forward to this year's platform and poster presentations. A special thank you to our invited speakers Esther Bullitt from Boston University and Jamie Warner from The University of Texas at Austin, for their support. I want to thank all corporate, honorary, regular, and student members for supporting the TSM with their membership and for participating at our annual meetings.

I am grateful for all the dedicated people who volunteer their time to take care of the Society. A big thank you to all the Executive Council members. Thanks to Amy Jo Hammet in her role as secretary of the TSM, Bernd Zechmann, our treasurer, for keeping the financial situation of our society in a good state. Thank you to James Long and Lyanna de Leon for representing our corporate and student members, and to Bernd Zechmann and Nabarum Gosh for taking care of our website and social media. Thank you to our journal editor, Catalina Pislariu, for organizing the review process, preparing, designing, and publishing of the Texas Journal of Microscopy.

Throughout 2023, the Executive Council worked hard to support our members, to make the TSM more visible, and our organization more efficient. In July, Josefina Arellano and Bernd Zechmann represented TSM as one of the Local Affiliated Societies of the Microscopy Society of America at the M&M meeting in Minneapolis, MN. We are enthusiastic about participating in future initiatives with MSA and we are happy to have a representative of the MSA Student Council at our 58th annual meeting in 2024. Stay tuned for more upcoming great projects.

Finally, I invite all TSM members to please run for office and volunteer for appointed positions. There are opportunities for everyone to make an impact in this community. We want to invite students, researchers, academic and industry partners, especially the new generations of microscopists, to make the TSM their society and drive it as a vibrant and engaging professional society for years to come.

*Josefina Arellano*

*TSM President 2023-2024*



# TEXAS SOCIETY FOR MICROSCOPY 58<sup>TH</sup> ANNUAL MEETING

## INVITED SPEAKER

### FINDING WAYS TO INHIBIT TRAVELER'S DIARRHEA USING CRYO-EM, IMAGE PROCESSING, AND OTHER BIOPHYSICAL METHODS

#### ESTHER BULLITT

Associate Professor

Department of Pharmacology, Physiology and Biophysics,  
Boston University Chobanian & Avedisian School of Medicine, Boston, MA, USA

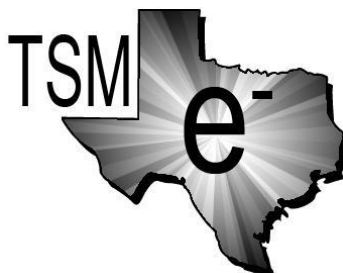
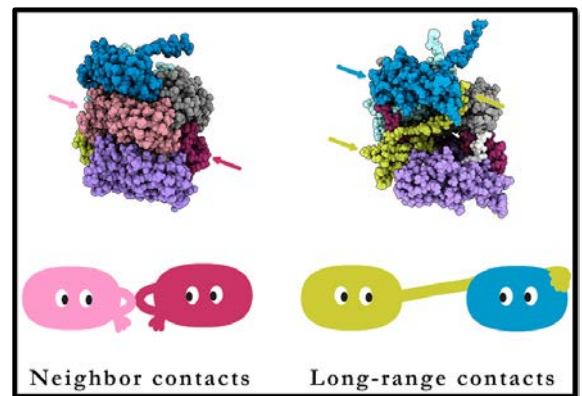


Using cryogenic electron microscopy (cryo-EM) and three-dimensional helical reconstructions, we are looking at virulence factors expressed on bacteria that cause Traveler's Diarrhea. The helical filaments, called "pili" or "fimbriae", are often essential for initiating infection, as they promote sustained adhesion of bacteria to the gut under adverse conditions.

Methods of cryo-EM and helical reconstruction will be discussed, leading to our current work on inhibiting adhesion of diarrhea-causing bacteria by a peptide in saliva, Histatin-5. It is well-known that salivary peptides play critical antimicrobial roles in human defenses against infection and inflammation of the mouth: small, histidine-rich, intrinsically disordered peptides are abundantly present in saliva and are active against oral pathogens that cause cavities, gum disease and thrush. The inhibitory effect of Histatin-5 against enterotoxigenic

Escherichia coli (ETEC) that cause Traveler's Diarrhea suggests a much broader role for these peptides in protecting human health.

Dr. Esther Bullitt is an Associate Professor in the department of Pharmacology, Physiology & Biophysics at the Boston University Chobanian & Avedisian School of Medicine. She has been a Biological Director and the 2020 President of the Microscopy Society of America. Her work on understanding infectious disease has included structural studies of macromolecules from bacteria and viruses, as well as investigating changes that occur in human cells, because of these infections.



# TEXAS SOCIETY FOR MICROSCOPY 58<sup>TH</sup> ANNUAL MEETING

## INVITED SPEAKER

### ADVANCED TRANSMISSION ELECTRON MICROSCOPY THROUGH PIXELATED DIRECT ELECTRON DETECTORS

JAMIE H. WARNER

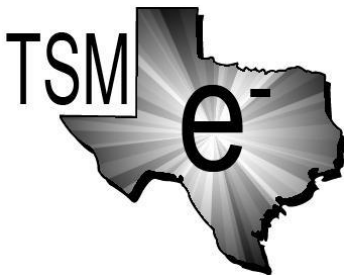
Professor

Department of Mechanical Engineering, The University of Texas at Austin, Austin, TX, USA



High speed pixelated direct electron detectors have transformed the way data can be captured in the transmission electron microscope, opening up new 4D-STEM methods and providing high sensitivity EELS measurements. In this talk, I will discuss how 4D-STEM can be used to image materials' atomic structure beyond conventional imaging approaches. This will include resolving the electric fields around single atoms in 2D Materials, such as graphene and MoS<sub>2</sub>, revealing new insights into charge density variations in defects, including dislocations. I will discuss how placing a direct electron detector in EELS system can enable studies at the zero-loss region and also measure energy loss out to large eV ranges. By combining in-situ heating holders, it is possible to obtain clean 2D material surfaces free from contamination and use 4D-STEM to detect line defects, point vacancies, and simultaneous low/high Z element imaging. This is applied to nanopores and edges, to reveal carbon atoms, as well as position averaged CBED measurements of Moire superlattice structure. In particular, I will discuss the quantitative aspects of 4D-STEM by comparisons to DFT calculations and simulations, which leads to the ultimate goal of mapping valence electron distributions in materials.

Dr. Jamie H. Warner is the Director of the Texas Materials Institute, which contains the Electron Microscopy Facility located in the Cockrell School of Engineering at the University of Texas at Austin. His research focuses on the next generation of nanostructured materials with unique properties that will impact electronic, opto-electronic, and energy applications. The core foundation of his research is on the atomic level structure and dynamics of nanomaterials realized through state-of-the-art aberration-corrected transmission electron microscopy and spectroscopy. He has received multiple Fellowships and awards. He is the Editor-in-Chief of the journal *Materials Today Advances*. His publications include more than 330 peer reviewed articles, including *Science*, *Nature Materials*, *Nature Nanotechnology*, *Nature Communications*, *Nano Letters*, *Advanced Materials*, *ACS Nano*, on the topics of nanomaterials for opto-electronics, energy, bio-applications, and quantum materials.



---

---

# Abstracts

---

## LIFE SCIENCES Spring 2024

### A COMPARTIVE MICROSCOPIC ASSESSMENT ON AEROALLERGEN OF TWO CITIES, AMARILLO AND ALBUQUERQUE. BEATRIZ BURCIAGA, AUBREY HOWARD, NABARUN GHOSH

Department of Life, Earth & Environmental Sciences, West Texas A&M University, Canyon, Texas 79015.

Aeroallergens have become a global concern causing more people to suffer more health effects due to pollen and mold. Scientific research and analysis of data on aeroallergen, asthma and allergic rhinitis revealed that environmental factors contribute to a high concentration of aeroallergen that led to the increased allergy cases all over the world (World Allergy Congress, Dec. 2023). Aeroallergens are foreign substances that include pollens, fungal spores, dusts, plant fibers, burnt residues and plant products like gums and resins. Aeroallergens cause serious allergic and asthmatic reactions characterized by sneezing, nasal itching, watery eyes, and other associated symptoms. This investigation aims at comparing the aeroallergen concentration of two adjacent areas with different topography, vegetation, and climatic conditions. We focused on the comparative aeroallergen indices and compared the concentrations of the specific pollen and mold spores that are prevalent in Albuquerque, NM, and the Amarillo-Canyon Metroplex of the Texas Panhandle for 4 years. The purpose was to compare the daily pollen and mold spore indices with the changes in the climatological conditions and incidences of forest fire. The analysis of air was performed through the collection of pollen and mold spores using a Burkard Volumetric Spore Trap, that is located on the third floor of the Natural Science Building of West Texas A&M University. The exposed tapes from Burkard Volumetric Spore Trap were stained and mounted with Safranin-Gelvatol mixture and were observed using an Olympus BX40 microscope equipped with FITC, TRITC filters, a mercury lamp source, a DP-74 digital camera. Aeroallergens were viewed, recorded and analyzed with CellSens software. We have received the aeroallergen data regularly by e-mail from the City of Albuquerque. In both the cities, the most significant aeroallergens recorded were the pollens like grass pollen (*Poaceae*), short ragweed (*Ambrosia artemisiifolia*), Scots pine (*Pinus sylvestris*), common sunflower (*Helianthus annuus*), hairy sunflower (*Helianthus hirsutus*), buffalo-bur (*Solanum rostratum*), purple nightshade (*Solanum*

*elaeagnifolium*) and lamb's quarters (*Chenopodium album*) and the fungal spores like *Alternaria*, ascospores from *Pezizales*, *Drechslera*, *Stachybotrys*, *Cladosporium*, *Curvularia*. In both cities, the meteorological conditions had direct influence on the aeroallergen concentrations. Temperature was found to have an inverse relationship with mold spore concentration. Rainfall was found to affect the mold count directly, with increases in precipitation bringing subsequent higher mold spore concentrations. Ragweed is the major culprit, but others of importance are sagebrush, red-root pigweed (*Amaranthus retroflexus*), lamb's quarters (*Chenopodium album*), Russian thistle (tumbleweed), and English plantain. Grasses and trees, too, are important sources of allergenic pollens. Trees that produce allergenic pollen include oak, ash, elm, hickory, pecan, box elder, juniper and mountain cedar. A significant correlation was evident between the aeroallergen indices and the patient visits. Anomalous shift in the aeroallergen was recorded in both the cities of Amarillo, Texas and Albuquerque, New Mexico.

### MICROSCOPIC ASSESSMENT OF THE GENETIC STABILITY FROM KARYOTYPING THE IN VITRO REGENERATED TREES AND MEDICINAL AND ORNAMENTAL PLANT SPECIES. BISWAJIT GHOSH<sup>1</sup>, SHAILY GOYAL<sup>2\*</sup> INDRANIL SANTRA<sup>1</sup>, NABARUN GHOSH<sup>2</sup>

<sup>1</sup>Plant Biotechnology Laboratory, Department of Botany, Ramakrishna Mission Vivekananda Centenary College, Rahara, Kolkata 700118 India. <sup>2</sup>Department of Life Earth and Environmental Sciences, West Texas A&M University, Canyon, Texas 79015.

In vitro regeneration of many plant species has become a standard technique for the propagation of the plants via plant tissue culture. Micropropagation is considered an important approach for the large-scale propagation of plants. It is especially significant for the improvement of those plants that prefer vegetative mode of reproduction. Conservation and multiplication of trees is one of the most important strategies that were undertaken to ensure the sustainability of the biosphere. Our lab has focused on multiplication via in vitro propagation of some economically important tree species, namely, *Albizia lebbek* (L.) Benth, (Shirish), *Albizia falcataria* and *Dalbergia sissoo* (Sisso). We have used various concentrations and combination of the plant hormones and growth supplements to induce

the regeneration of plantlets via callus formation and embryogenesis. We used a SZ-40 Stereomicroscope to observe the stages of regeneration in vitro. For the tree species, we found that the hypocotyl and cotyledon explants exhibited the maximum regenerative capacity on using 6-Benzylaminopurine (6-BAP), Indole-3-Acetic Acid (IAA), Indole-3-Butyric Acid (IBA), and 2,4-D (2,4 Dichloro-phenoxy Acetic Acid). Addition of coconut milk (v/v) proved to be beneficial for in vitro regeneration of the tree species.

The lack of sexual reproduction in most of the members of *Zingiberaceae* hampered the response of the plants to conventional breeding. Moreover, the poor multiplication of rhizomes and high susceptibility to physiological and temperature stress during storage push them beyond any conventional technique applied for crop production. Hence, in vitro techniques proved to be a valid choice for large-scale production and quality improvement of the Indian ginger plants. Prior to micropropagation, aseptically establishment of the explant in in vitro system is obligatory. Plant tissue culture is now indispensable for the large-scale production of genetically identical rare plant genotypes that have remarkable commercial applications. Different approaches to in vitro propagation are the best alternatives for the mass production and conservation of Indian gingers. This joint investigation (Dr. N. Ghosh & Dr. B. Ghosh's Labs in USA and India) is focusing on different in vitro aspects including updated micropropagation status of important tree species, medicinally and ornamentally important Indian species that would ultimately help in the conservation of indigenous germplasm.

Rhizomatous explants exhibited a better rate of micropropagation instead of the leaf segments cultured on the MS medium (Murashige and Skoog, 1962) supplemented with 2, 4-D. The source of explant is an important factor in the formation of callus. The frequency of shoot induction from callus was enhanced when higher concentrations of cytokinin and lower concentrations of auxin were used cordially in the medium. Carbon source is an important parameter in plant tissue culture to maintain osmotic environments for a significant increase in shoot length and number. The presence of maltose, a non-reducing sugar proved to be the best carbon source for the multiplication of *Curcuma* species. Somatic embryo formation and maturation are also directly affected by the varied strength of carbon source present in the medium. Thidiazuron (TDZ) is a cytokinin-like compound used in in vitro plant tissue culture for regeneration and shoot proliferation which is about 100 times more efficient than conventionally used cytokinins to induce micropropagation. The combination of TDZ with 2, 4-D, and BAP proved to be best for somatic embryogenesis in *C. amada*. Carbendazim is also a cytokinin-like compound that can cause shoot elongation without harming the explant in *C. longa*. The combination of NAA and BAP proved to be the best

combination for micropropagation in different species of *Zingiberaceae* including *C. aeruginosa*, *C. amada*, *C. caesia*, *C. longa*, *H. coronarium*, and *K. galanga*.

*Coleus scutellarioides* (L.) Benth. is a very popular ornamental plant with attractive colorful foliage and also has several medicinal properties. A detailed cytogenetic study was conducted in the 'Red Trailing Queen' horticultural form of this species. Recent reports on the cytogenetic assessment of this species is meager, hence a reassessment and detailed cytogenetic study of this species are necessary. The karyotype study revealed that somatic cells contain  $2n=48$  small chromosomes, classified into metacentric to submetacentric. Meiotic chromosomes stained with acetocarmine and 4',6-diamidino-2-phenylindole (DAPI) revealed the occurrence of univalent, bivalent, and multivalent associations of chromosomes along with secondary associations. The result confirms the allopolyploid origin of this plant. Meiotic irregularities like laggard chromosomes and multipolarity movement have also been found. In addition to that, variation in the chromosome numbers within pollen mother cells (PMCs) has been observed frequently. Pollen viability has been determined by fluorescein diacetate (FDA) and found to be very low. Rosmarinic acid (RA) is a natural polyphenol utilized as an anti-microbial, immunomodulatory, anti-diabetic, anti-allergic, anti-inflammatory, hepato-protectant, and renal-protectant agent. The RA content has been quantified through high-performance liquid chromatography (HPLC) to find out the medicinal efficacy. The present investigation on the detailed cytogenetics study along with the pollen viability will be beneficial in the breeding program and accordingly useful in further improvement of this ornamental medicinal plant. Karyotype analysis of the regenerated plantlets is a standard cytological analysis, that is done to assess the genetic stability of the regenerants. We have analyzed the karyotypes of all the regenerated plants to confirm their genetic stability.

## **TWU POLLINATOR GARDENS AS SIGNIFICANT SOURCES FOR STUDENT MICROSCOPY PROJECTS. CAMELIA MAIER**

Division of Biology, School of the Sciences, Texas Woman's University, Denton, Texas 76204

Plant-pollinator interactions are affected by global change, with largely negative impacts on pollination, crop yields, and food supply for an exponentially growing human population. Native urban gardens contribute to the conservation of native pollinator populations, most of which are in decline. Texas Woman's University (TWU), promoting sustainability education and civic engagement, has restored two campus areas into native pollinator habitats to support dwindling populations of Monarch butterflies, native bee species, and other pollinators. The

pollinator gardens give students many opportunities to 'learn by doing' and support their research activities. Students are observing plants, insects and even pathogens in the gardens, choose a research topic, are trained on using light and scanning electron microscopes (LM and SEM), obtain results, and present them at the annual TWU Student Creative Arts and Research Symposium and other regional and national venues. Most of the projects study the relationships between native plants and insect pollinators. Pollen is collected from flowers and pollinator bodies and microscopically observed for identifying flowers visited and for building a network of plant-pollinator relationships. Insect pollinators are also observed with LM and SEM and their adaptations for feeding on nectar and collecting pollen, if the case, are discussed, activity which helps predict other species of plants that could be visited by the specific pollinators under study. One other project that students also are interested in pursuing is 'discovering' the nature of leaf spots. Goldenrod, *Solidago sp. (Asteraceae)* is a native plant in the TWU butterfly gardens that provides nectar for pollinators. Students observed high number of white leaf spots on the plants in the fall. Leaves were collected, dissected, and examined with LM and SEM. The white spot portion was filamentous and identified as *Botryosphaeria dothidea* fungus. Inside the filamentous structure, midge fly (*Asteromyia carbonifera*) larvae were identified. The microscopic study was followed by a literature search and students learned about a three-way symbiosis between the midge fly, fungus, and plant, mutualistic between larvae and fungus, parasitic between fungus and plant. Female midge flies inoculate fungal spores when they lay eggs inside the leaves and growing hyphae from spores provide food and protection for larvae by encapsulating them until they mature. Other popular microscopy projects involve studying the morphology of native plant seeds for the creation of a database that could serve scientists and gardeners as well. The newly established TWU butterfly gardens represent a significant resource for science project and sustainability education.

#### **MICROSCOPIC ASSESSMENT OF THE WATER QUALITY SHOWING THE PRESENCE OF CYANOBACTERIA AND USE OF *DAPHNIA* TEST SYSTEM TO DETECT THE EFFECT OF ATRAZINE.**

ANNA NGUYEN, MARYTRINH NGUYEN, MARIA ZAVALA, NABARUN GHOSH.

Department of Life, Earth and Environmental Sciences, West Texas A&M University, Canyon, Texas 79015

Water quality is an important criterion influencing the health of the public and wildlife in an area. Due to the consistently increasing fossil fuel use, global climate change and wastewater runoff, water quality in many cities continues to decline. In addition to the abundant growth in Cyanobacteria blooms, particulate

matter from chemicals used to counter the blooms such as algacides, hydrogen peroxides, and copper sulfate contribute to the decrease of water quality. Spraying or the direct dispersion of chemicals into our freshwater bodies reduces cyanobacteria, but the effect is only temporary. The constant cycling of such substances would eventually create an area where neither marine life nor plants can survive; such areas are referred to as 'dead' zones. If bodies of water were left alone to thrive under natural conditions, the highly concentrated and rapidly growing cyanobacteria would lead to murky waters, high oxygen consumption, cyanotoxins, strong odors, and a decrease in aquatic organisms forming anaerobic zones. Not only would the overgrowth of cyanobacteria and their cyanotoxins negatively affect marine life, but it could also cause serious health issues or even death for mammals and humans alike when ingested. Poisoning due to cyanobacteria toxins microcystins and cylindrospermopsins has taken more than fifty lives in Caruaru, Brazil in 1996, and, in 1983, a rural town in Australia was supplied with drinking water that carried toxic cyanobacterium eventually leading to severe hepatoenteritis in the population. Alongside the decrease of water quality and health, our agriculture and economics is also affected by the increase in cyanobacteria. Providing such water quality to our plants and animals in farms would either kill them off, result in diseases, and if consumed, would also decrease human health. Many will begin to look for other sources for their food and water, leading to a shift in the way our economic system is already setup. Water reaches us in many different ways such as in any products that we use for our bodies and sink and bath water. If the daily products and water we use is contaminated, this would inevitably lead to frustrating unhealthy lifestyles. Current strategies in an attempt to solve this problem is closely monitoring bodies of water and the removal of phytoplankton and cyanobacteria is more than 90% when filtered with the micro-strainer filtration water treatment; drones are also being equipped with sensors to detect early cyanobacterial blooms. Coagulants and minerals are still being experimented with in an attempt to get better results with less consequences of such materials being used. In our Aerobiology lab at West Texas A&M University, we have collected water samples from various locations in Amarillo-Canyon Metroplex, namely Southeast Water Park Lake, Ross Rogers Golf Course Lake, and Medical Center Park Lake. We prepared slides using the water sample added with a few drops of distilled water; on mounting with a cover slip we examined the slides under the microscope using the bright field, dark field, phase contrast, TRITC and FITC fluorescent filters to examine and characterize the samples. We found different types of Cyanobacteria in the collected water samples, the two major species were *Anabaena* and *Microcystis*. The *Anabaena* filaments showed the presence of heterocysts and akinetes that

were evidenced by using the FITC and TRITC filters with fluorescence, exhibiting their active growth phases. These can produce toxins that are poisonous to fish and wildlife that drink water contaminated with the toxins. Furthermore, there are documented cases of blue-green algal toxins harming humans in other parts of the world through the consumption of poorly treated waters. In the next part of the observation, we examined the effect of different doses of Atrazine on the *Daphnia* or water flea test system. Atrazine, a common herbicide for the broadleaf weeds, very widely used in the states of Texas and Minnesota in the agricultural practices. Water collected from the wells of Tulia, a city in the Texas Panhandle showed traces of Atrazine. It was detected in the lakes and water bodies that probably got contaminated by running rainwater from the crop fields. We used the Sedgwick Rafter (SR) Counter filled up with distilled water as the control set, 0.01%, 0.1% and 1% Atrazine prepared in the Laboratory following the serial dilution method. We observed the prepared SR Counter to detect the lethal doses (LD). In the control set, only 1-2% *Daphnia* showed lethality, whereas the LD50 or Lethal Dose 50 was recorded with the 0.1% Atrazine. Almost 100% *Daphnia* showed lethality proving thereby that 1% Atrazine is highly toxic to the livestock.

**MICROSCOPIC ANALYSIS ON CHANGES IN INDOOR AND OUTDOOR AIR QUALITY IN RELATION TO INSECT POPULATION AS A POTENTIAL CAUSE OF ALLERGIC REACTIONS.**  
MARYTRINH NGUYEN<sup>1</sup>, NABARUN GHOSH<sup>1</sup>,  
SHAILY GOYAL<sup>1</sup>, JAY VITALE<sup>2</sup>

<sup>1</sup>Department of Life, Earth and Environmental Sciences, West Texas A&M University, Canyon, Texas 79015. <sup>2</sup>Air For Life, Milton Keynes - MK12 5TS, Buckinghamshire, UK.

In present-day studies in allergy and asthma cases, it is important to observe the correlation of meteorological conditions with local aeroallergen composition. In addition to naturally occurring aeroallergens such as pollen, fungi, and particulate matter from wildfires or plant exudates, insect parts also contribute to increased particle pollution and can cause respiratory allergies including asthma and rhinitis. Insects can cause ailments by stinging, biting, or simply through their larvae and waste that is spread by contact with food, household items, and pets or animals. Allergy symptoms due to an insects' sting or bite include pain, swelling, redness, and itching though these are normal reactions that go away within a couple hours or days. Common allergy symptoms that are not related to bites or stings can cause sneezing, coughing, runny or stuffy nose, and itchy eyes, nose, mouth, or throat and can last longer durations ranging from weeks to months. Allergic reactions to insect parts can also be life threatening, resulting in

skin rashes, swelling of lips, tongue, or throat, shortness of breath and difficulty breathing, serum sickness, toxic reactions to the insect venom, dizziness, fainting, seizures, stomach pain, vomiting, bloating, diarrhea, and death. Insect parts can become airborne and adhere to other aeroallergens such as fibers, plant exudates, burnt residues, pollen and fungi can be carried long distances. Patients with asthma or rhinitis are especially vulnerable to exposure to insect populations both indoor and outdoor. Common indoor insect populations include bedbugs, cockroaches, booklice, dust mites, and various beetles that cause ailments from within the home. Common outdoor insects include moths, crickets, locusts, caddis flies, midges that cause increased seasonal allergies from Spring to Autumn. In some cases, they are found both indoors and outdoors as evident with *Drosophila* fruit flies and Asian lady beetles which are outdoor insects that invade houses and cause many allergy cases in the United States. In our Aerobiology research lab, NSB-215, outdoor air samples have been obtained using a one-sided sticky tape wrapped around a drum of a Burkard Volumetric Spore Trap placed on the roof of the Natural Science Building at West Texas A&M University. The samples were then mounted into slides for microscopic examination for insect parts also including fibers, plant exudates, and PM2.5 through a BX-40 Olympus microscope for analysis. In some of our slides, insect parts appear whole or broken into pieces and we have observed scattered scales from the insect's body and wings. To further assess the prevalence of insect population, present in indoor air and its response to air purification techniques, our Aerobiology lab conducted a simulated experiment in a fiberglass chamber using the AFL Mini Air Sanifier and a Lighthouse Handheld Particle Counter to assess indoor air quality. This equipment measures the Particulate Matter (PM) concentration of varying sizes. At different intervals, we recorded a decrease in concentration of PM2.5 when using the air purifier and compared with data collected from counts without running the air purifier. The AFL Mini Air Sanifier has been shown to help reduce PM2.5 and improve indoor air quality by using AFLPCO nanotechnology. Research on insect populations and their effects in conjunction with other aeroallergen is necessary to improve overall indoor and outdoor air quality. Using advanced air purification techniques alongside preventative measures to limit patient exposure to insects through contact, inhalation, ingestion, bites or stings can possibly lower total instances of allergenic reactions. With the current unprecedented situation of the "spread of bedbugs" in the indoor environment of residential, hotel and all dwelling facilities have become a major concern in many Asian and European countries especially in the UK. Even after repeated dry cleaning and washing the bedding materials with hot water, people are facing the problem with bedbugs in different countries of the world. There is a great demand for an energy efficient

air purifier that cleans up the bedding materials at the site by targeting the insect pests efficiently. With the revolutionary, energy-efficient technology, the filterless AFL Mini II® fights all kinds of impurities by cleaning and sanitizing the air including all the surfaces in a room up to 330 square feet. The researchers at the West Texas A&M University have set up equipment for testing the effect of using the AFL Mini Sanifier II® in a simulated environment of a fiberglass chamber in the Aerobiology Lab, NSB-215. We used an insect test system to determine the efficacy of this negative ion air purifier in reducing and eradicating the bedbugs. *Drosophila melanogaster* (fruit fly) is an insect and a widely used model lab organism. The similar size of the fruit fly and the bed bug justifies the usage of the fruit flies as the model organism for this testing. The actively growing culture of the *Drosophila* sp. or the fruit fly was purchased from the Wards Biological Supply. The AFL- Mini Sanifier II® was assessed for their efficacy in eradication of the bedbugs was carried out by the researchers in the West Texas A&M University for an efficient use of the AFL air purifiers in maintaining the hygiene of the indoor environment. The experiment carried out using a fiber glass chamber placed in the Aerobiology Lab. To begin the experiment, we set up the equipment into the fiber glass chamber by placing the AFL Mini Sanifier II®, the Air Purifier, Lighthouse Air Quality meter and two fans on two sides of the chamber. We collected the fruit flies after knocking them out briefly keeping them in a refrigerator for 5-10 minutes. This process keeps the fruit flies alive making them unable to fly. We counted the number of living flies on placing them on the Petri-plates and observing them under the dissecting scope, SZ-40 and a stereomicroscope, AmScope. We placed the living flies on the Petri dish with a standard counted number of 50 in each Petri dish totaling a number of 100 and placed the Petri dishes at the center of the fiberglass chamber for further experimentation and observations. We ran the fans with the lowest speed to provide aeration to the knocked-out flies to after opening the top part-cover of the Petri dishes. On providing aeration the fruit flies became active and moved to different parts of the fiberglass chamber. We ran the air purifier for 24, 48, 72 and 120 hours. We counted the living and dead samples of flies at every interval. We calculated and measured their subsequent lethality by counting the living and dead samples on using the AFL air purifier. The experimental procedure was repeated three times and the average of all the data were taken for consideration. We captured images at various steps and tabulated the data and analyzed them statistically on lethality induced by the air purifier at different interval and made an excel graph to show the efficiency of the air purifier in eradication of the testing insects, the fruit flies. The experiment has demonstrated the efficiency of the AFL Mini II® Air Purifier in eradication of the similar insect model fruit fly (*Drosophila* sp.) justifying the usage of the same equipment in controlling the bed bugs by destruction

and complete eradication of them since, it was capable of inducing high level of lethality in the similar size insect used in this test by the researchers at the Aerobiology Lab. The researchers also recommend a continuous running of the AFL Mini II® and monitoring the bedbugs for a complete eradication.

## ASSESSING THE TOXICITY OF PERFLUOROOCCTANOIC ACID, AND PERFLUOROBUTANOIC ACID IN HUMAN GUT AND NEURONAL CELLS USING CLSM AND SEM. PRECIOUS C. OBIAKO, SOLOMON O. AYISIRE, CHRISTIE M. SAYES

Department of Environmental Science, Baylor University, Waco, TX 76706

Drinking water is a significant source of exposure to per- and polyfluoroalkyl substances in humans. The chemicals have garnered attention from environmental health scientists due to their pervasive presence, recalcitrant nature, deleterious health effects, and regulatory scrutiny. Acceptable exposure concentrations for humans have been established based on the potency of each specific pollutant. A more realistic exposure scenario for these substances, though, involves simultaneous exposure to long-chain (perfluorooctanoic acid (PFOA)) and short-chain (perfluorobutanoic acid (PFBA)) variants.

This study evaluated the cytotoxicity of individual and binary exposures to PFOA and PFBA against human colon (Caco-2) and neuronal (SH-SY5Y) cells. Mitochondrial toxicity was assessed using fluorescence staining and confocal laser scanning microscopy (CLSM) and supplemented with metabolic activity (MTS), ROS (ROS-Glo™), and extracellular flux (Seahorse XFp Analyzer) assays. Scanning electron microscopy (SEM) was also used to evaluate the morphological features of the cells post-exposure. Our findings show that, compared to PFBA, PFOA induces more toxicity (cellular and mitochondrial) in both cell types tested. The possible mode of toxic action is through increased oxidative stress over time, as indicated by a significantly higher amount of ROS. Preliminary data shows that the chemical interactions between PFOA and PFBA caused a synergistic cellular response. The study presents convincing evidence that exposure to mixtures of per- and poly-fluoroalkyl substances may induce different toxicities than individual chemicals alone. It is necessary to re-evaluate the acceptable exposure concentrations of pollutant mixtures in drinking water.

**DYNAMICS OF SHEATH PROTEIN OF A MYOVIRIDAE COLIPHAGE DURING HOST INFECTION STUDIED USING INDUSTRY SPECIFIC CLOUD COMPUTING RESOURCES.**

ANINDITO SEN<sup>1</sup>, GREGORY G. SERVOS<sup>2</sup>, LE TRAN<sup>2</sup>  
<sup>1</sup> Microscopy and Imaging Center, Texas A&M University, College Station, TX 77843; <sup>2</sup> Ovation Data Services, Inc., Houston, TX 77041.

The sheath protein of a *Myoviridae* phage is a unique microinjection device that compresses to ~52% of its original length during its host infection. The compression is not uniform, where the sheath subunits undergo significant conformational change that initiates at the tail-baseplate interface and gradually spreads to the subunits up towards the capsid, as the phage performs a cork-screw type downward motion, infecting its host. Given this compression is tremendously expeditious, only a handful of images are recorded for some of the microinjection devices to explain this phenomenon, (Maghsoodi et al., 2019). Here, we have employed cryo-

TEM images followed by cloud based computational image analysis of P1 coliphage, to determine the entire motion of the sheath tube during the infection process. Movies of the P1 are recorded on a Glacios cryo-TEM equipped with a direct electron detector from ThermoFisher Scientific and are uploaded to the cloud compute and storage of Ovation Data where they are worked upon by a series of image reconstruction software to generate 3-Dimensional (3D) electron density maps of the different states of the sheath tube. The maps are then computationally worked upon to generate the entire 3D state of the compression in a movie format. The 3D reconstruction process, carried out on the cloud is controlled by a cellular device using an app on it that is directly linked to the server (Figure 1). The outcome of this study joins the results of a small group of 2 other microinjection macromolecular complexes (T4 phage and R-type bacteriocin) whose sheath conformational changes during the intermediate states of infection have been studied during the infection process (Maghsoodi et al., 2019; Frazer et al., 2021).

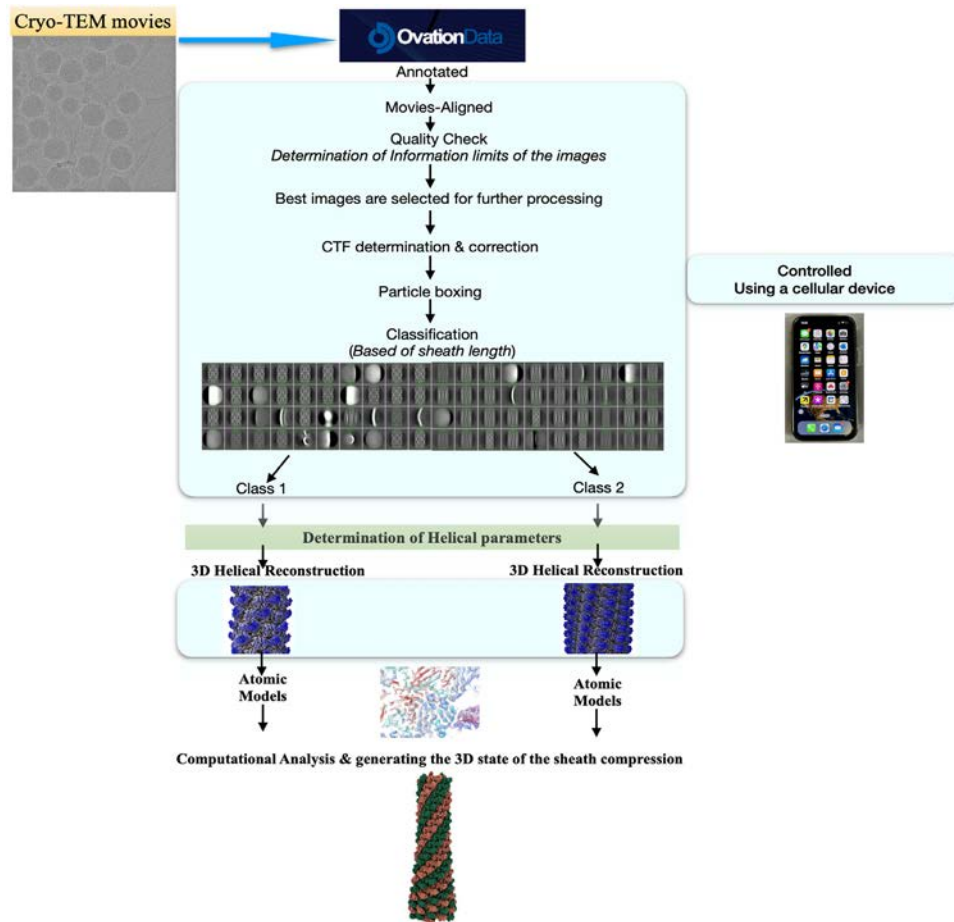


**Figure1.** Workflow for the 3D reconstruction of the sheath protein of P1 coliphage.

**References:**

Maghsoodi, A., A Chatterjee., I. Andricioaei and N.C. Perkins. How the phage T4 injection machinery works including energetics, forces, and dynamic pathway. *PNAS*, 2019, 25, 116(50),25097-25105.  
 Frazer, A., N.S. Prokhorov., F. Jiao, B.M. Pettitt., S. Scheuring., P.G. Leiman. Quantitative description of a contractile macromolecular machine. *Sci. Adv.* 2021, 7, 2.

**SPACE-AGE SOLUTIONS: ADDRESSING MICROBIAL CORROSION WITH AI-DRIVEN IMAGE ANALYSIS.** EVAN ORTIZ, ROBERT MCLEAN, JELENA TESIC, STARLA THORNHILL, ANDREW SCOUTEN.

Texas State University, Department of Biology, San Marcos TX 78666

Microbial-induced corrosion (MIC), due to biofilm formation on metallic surfaces, presents a critical challenge in maintaining water systems on Earth and in space missions. The Water Recovery System onboard the International Space Station relies on chemical and physical methods to mitigate biofilm formation, which then ensures safe drinking water for the crew. Microorganisms within this system and associated biofilm formation pose a risk to astronaut health and system integrity due to potential MIC. This research leverages recent advances in machine learning and computer vision to develop innovative tools for scientific image analysis based on scanning electron microscopy (SEM). During Spaceflight CRS-21, stainless-steel coupons were exposed to a biofilm-forming mixed culture of *Escherichia coli* and *Pseudomonas aeruginosa* then fixed in paraformaldehyde after 16-, 26-, and 117-days incubations, with a 32-hour delay for ground controls. Following retrieval, the coupons were examined by SEM. Expert labeling of the MIC affected regions in the SEM images, served as the training images for the neural network. Initial results using feature extraction and pattern recognition showed promising accuracy with an intersection over union score of 44.59% and an average Dice score of 55%. Future work in conjunction with data from the most recent flight experiment on CRS-29 will focus on refining the neural network and expanding the sample size to enhance the accuracy and applicability of our findings in space missions.

**CO-LOCALIZATION ANALYSIS: DOES PAX6 BIND CYTOSKELETAL ELEMENTS?** NISA SINDHI<sup>1</sup>, BRITTANY DOBBINS<sup>1</sup>, RUBEN TOVAR<sup>2</sup>, DANA GARCIA<sup>1</sup>

<sup>1</sup>Department of Biology, Texas State University in San Marcos, 601 University Dr, San Marcos, TX 78666,

<sup>2</sup>Department of Integrative Biology, The University of Texas at Austin, 2415 Speedway, Austin, TX 78712

To identify protein interactions, many tools come in handy; one of them is co-localization analysis using a confocal microscope. Here we assay for co-localization of PAX6 protein with cytoskeletal elements. PAX6 is a well-known transcription factor essential for the development of tissues including the eyes, central nervous system, endocrine glands, and salivary glands of vertebrates and invertebrates. PAX6 is highly conserved across the animal kingdom. Our group discovered that PAX6 localizes within the mechanosensory neuromasts of the lateral

line system in paedomorphic, *Eurycea salamanders*, namely *E. nana*, *E. sosorum* and *E. rathbuni*. We used polyclonal and monoclonal anti-PAX6 antibodies in immunohistochemical studies. This finding represents the first, nonpathological documentation of the extranuclear localization of PAX6, with intense antibody labeling in the apical appendages of the hair cells of the neuromast. This finding suggests PAX6 co-localizing with cytoskeletal elements, as apical appendages consist of microtubule-filled kinocilia and actin-filled stereocilia. We used Alexa Fluor 488 phalloidin dye to stain F-actin, and DAPI to stain the nuclei. The localizing regions of PAX6 and F-actin are the preliminary evidence of our hypothesis. Based on the results of co-localization using a confocal microscope, we aim to conduct supporting biochemical assays to corroborate our findings.

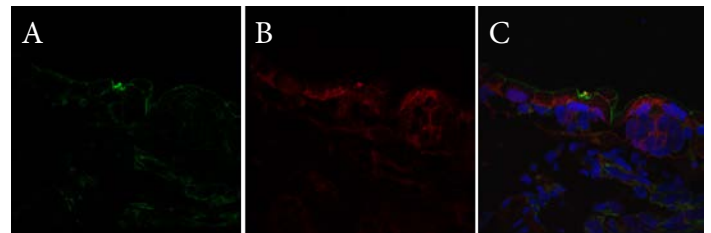


**Figure 1:** Neuromast from a lateral line of San Marcos salamander (*Eurycea nana*) imaged at 60X magnification and presented as a Z-stack. A) F-actin labeled with Alexa fluor 488 phalloidin (green); B) PAX6 labeled with PAX6 polyclonal antibody (red); C) merged image of F-actin, PAX6, and nuclei (blue) stained with DAPI.

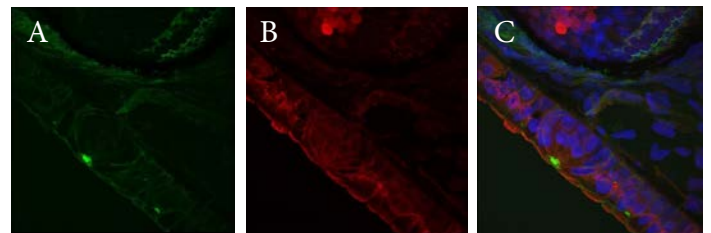


**Figure 2:** Neuromast from a lateral line of San Marcos salamander (*Eurycea nana*) imaged at 60X magnification and presented as a Z-stack. A) F-actin labelled with Alexa fluor 488 phalloidin (green); B) PAX6 labeled with PAX6 recombinant rabbit monoclonal antibody (red); C) merged image of F-actin, PAX6, and nuclei (blue) stained with DAPI.

**CANCER CELL TARGETING VIA SELECTIVE TRANSFERRIN RECEPTOR LABELING USING PROTEIN-DERIVED CARBON DOTS.** SARA STRICKLAND, MYCHELE JORNS, LUKE FOURROUX, LINDSEY HEYD, DIMITRI PAPPAS

Department of Chemistry and Biochemistry, Texas Tech University, Lubbock, TX 79409

Carbon based nanoparticles such as carbon dots (CDs) have had a recent surge in popularity as a fluorescent probe due to their immense advantages in bioimaging and biosensing. However, CDs lack affinity

and specificity for biomolecules limiting their practical applications in bioimaging, targeted therapeutics, cytometry, etc. To overcome this limitation, we report transferrin receptor (CD71) targeting affinity fluorescent CDs. These affinity nanoparticles are directly synthesized with direct tuning of nanoparticle affinity via simple and careful precursor selection of a protein which possesses a function of interest. We hypothesized that the original protein's peptides are preserved on the surface of the CD enabling selective binding to the protein precursor's receptor. Affinity-based cell assays and spectroscopic characterization techniques such as Fourier Transform Infrared Spectrometry (FTIR) confirmed the retention of precursor affinity. The precursor transferrin was utilized to produce transferrin derived CDs which show affinity

for CD71, a well-known cancer biomarker that is highly expressed in nearly all cancer cell lines as the main uptake pathway for cellular iron. The affinity cell assays were conducted using the human leukemia cell line HL60 and demonstrated selective targeting of CD71 by the affinity CDs, specifically by triggering transferrin-mediated endocytosis via clathrin-coated pits. Spectroscopic characterizations of the nanoparticles show bright violet fluorescence, 7.9% quantum yield in aqueous solution. The capacity of this method to simply and efficiently tune nanoparticle affinity based on precursor selection strongly indicates that this process can be repeated for other disease biomarkers, hereby enabling practical application of affinity CDs in biosensing, diagnostic bioimaging and target therapeutics.

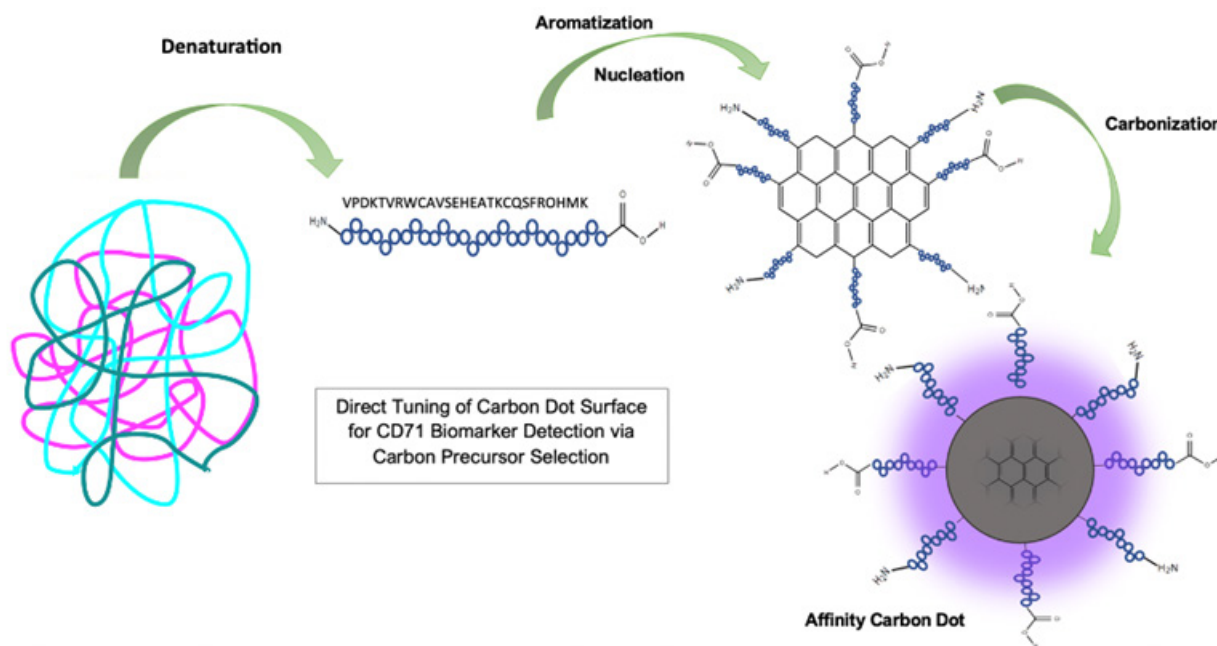


**Figure 1:** Proposed mechanism of affinity carbon dot nanoparticle formation. Proteins are initially denatured. Then, the amino acid sequence is aromatized as carbon-carbon bonds form. Then, nanoparticle nucleation begins. Fresh carbon-carbon double bonds continue to form as carbonization of the amino acids at the surface of the particle takes place. When the heating is terminated before complete carbonization, the resulting violet fluorescent particle will possess a graphene-like core with an amino acid functionalized surface.

## MATERIAL SCIENCES Spring 2024

**EFFECT OF STATE-OF-CHARGE ON PARTICLES EJECTED FROM LITHIUM-ION BATTERIES DURING THERMAL RUNAWAY.** DAVID M. MILLER, CHRISTIAN A. LANDRY, PAUL O. ADEFIRANYE, SAMUEL A. MCCAULLEY, JAMES C. THOMAS., J. Mike Walker '66 Department of Mechanical Engineering Texas A&M University, College Station, Texas, 77845

Lithium-ion batteries (LIBs) are utilized for a variety of energy storage purposes and have seen continual

growth into different technological sectors due to their attractive properties. This has resulted in an increase in safety concerns regarding the thermal runaway (TR) of LIBs and its implications on consumer health. TR is the result of the catastrophic failure of a LIB that can occur via mechanical, thermal, or electrical abuse and can lead to the combustion of the battery. The creation of toxic and/or flammable gases, significant energy release, jet flames, ejection of particulates, and secondary explosions are several hazards presented during a LIB TR event that pose major safety hazards to consumers in the vicinity. In order to study these hazards, a state-of-the-art LIB TR experiment was developed at Texas A&M University that thermally initiates TR and safely contains the event. The current study investigates the particles ejected from

LIBs during TR at different state-of-charges (SoCs) with microscopy and materials analysis techniques. A battery's SoC is a relative measure of the amount of energy being stored within it and this research seeks to understand its relation to the characteristics of the particles ejected from a LIB during TR. The studied LIB cell is a Panasonic NCR 18650B that is characterized by its lithium cobalt oxide (LCO) cathode material. Three of these cells at 0%, 50%, and 100% SoC underwent TR in an atmosphere of air under ambient conditions. Previous work by Landry et al., 2023, studied the particles ejected from the Panasonic battery at 100% SoC. It was found that a micro- (< 1  $\mu\text{m}$ ) and macro- (~ 2mm) particles were present in scanning electron microscopy (SEM) imaging. Additional elemental dispersive spectroscopy (EDS) highlighted the elemental dispersion on the surface of a representative particle and provided evidence of reactions that took place with the battery's components. A materials analysis was performed using x-ray power diffraction (XRD) and x-ray photoelectron spectroscopy (XPS) techniques to determine specific compounds created by the TR reaction. Partial oxidation of metallic compounds from the LIB were seen along with products formed from reactions between the battery's components. This work sets the framework for the analysis of the 0% and 50% SoC particles. An understanding of the fundamental LIB TR reactions and their relationship to SoC may be derived from this work. These findings will provide valuable insight into LIB safety research and ultimately lead to the development of safer LIBs.

#### References:

Landry, A. C., Adefiranye, O. P., McCaulley, A. S., and Thomas, C. J. Characterization of Ejected Particles from a Lithium-Ion Battery During Thermal Runaway," *Texas Journal of Microscopy* 2023, Vol. 54, No. 1, pp. 18-19.

### SYNTHESIS OF PURE MAGNESIUM NANOPARTICLES BY PULSED LASER ABLATION IN TRITON X. STEPHEN BLISSETT, TINA HESABIZADEH, GRÉGORY GUIBBIERS.

Department of Physics and Astronomy, University of Arkansas at Little Rock, AR 72204

Magnesium (Mg) is the eighth most abundant chemical element on earth, and the prospect of developing lightweight materials based on magnesium is currently a hot topic. The Mg nanoparticles were synthesized by pulsed laser ablation in liquids (PLAL). The laser used in this synthesis was a nanosecond Nd: YAG laser emitting at 1064 nm. The laser beam was reflected onto a gold-coated mirror, inclined at 45° relative to the laser rail, and directed "top-down" toward the pure Mg target. The Mg target (from Plasmaterials, USA) is pure @ 99.98% and was sitting within a 50 mL single-neck rounded flask and filled with 5 mL of Triton X-100 (from Fischer Scientific Company, USA). Triton X-100 was used

undiluted, as a 100% pure solvent at room temperature. Triton X-100 is a non-ionic surfactant with the following chemical structure,  $(\text{C}_{14}\text{H}_{22}\text{O}(\text{C}_2\text{H}_4\text{O})_n)$ . The laser beam was focused by a biconvex lens (focal length = 83 mm) and the target was irradiated for 30 min. The repetition rate of the laser was fixed at 1 kHz with an energy output of 5.5 mJ/pulse. The microscopy study determined the spherical shape of the Mg nanoparticles as well as their size distribution around ~100 nm. Furthermore, it confirmed that Triton X protected Mg nanoparticles from oxidation.

#### References:

Soheil, S., Blissett, S., Raji, H., Hesabizadeh, T., Osterlin, B., Guisbiers, G. Enhanced elasticity in magnesium nanoparticle reinforced acrylic elastomer. *Polymer Engineering & Science* 2023, 63, no. 10: 3223-3230.

### SYNTHESIS OF TeO<sub>2</sub> NANOPARTICLES BY PULSED LASER ABLATION IN LIQUIDS. T. HESABIZADEH<sup>1</sup>, G. GUIBBIERS<sup>2</sup>

<sup>1</sup>Department of Biology, University of Arkansas at Little Rock, Little Rock, AR 72204; <sup>2</sup>Department of Physics and Astronomy, University of Arkansas at Little Rock, Little Rock, AR 72204

This research outlines the synthesis of tellurium dioxide (TeO<sub>2</sub>) nanoparticles using the bottom-up approach with pulsed laser ablation in liquids (PLAL). The process was guided by a nanosecond Neodymium-doped Yttrium Aluminum Garnet (Nd:YAG) laser operating at 1064 nm, irradiating a Te target immersed in deionized water (Hesabizadeh et al., 2022). A precise 5-minute irradiation period at 1 kHz resulted in the successful synthesis of spherical  $\alpha\text{TeO}_2$  nanoparticles with sizes ranging from 6.5 and 150 nm. Comprehensive characterization techniques, including electron microscopy, and diffraction, allowed us to scrutinize these nanoparticles in detail. We observed the spherical morphology and validated the findings through Electron Microscopy. Furthermore, we highlight the intriguing chemistry behind this process, revealing Te's affinity for oxygen bonding. The bottom-up synthesis powered by the laser-target interaction, showcases its potential for nanoparticle production as an alternative method to reduce waste and increase efficiency. TeO<sub>2</sub> nanoparticles hold promise across diverse applications in science and technology, from optics to materials science, presenting an exciting frontier in nanofabrication.

#### References:

Hesabizadeh, T., Hicks, E., Medina Cruz, D., Bourdo, S.E., Watanabe, F., Bonney, M., Nichols, Webster, T.J., Guisbiers, G. Synthesis of "Naked" TeO<sub>2</sub> Nanoparticles for Biomedical Applications, *ACS Omega* 2022, vol. 7, 23685-23694.

## **SYNTHESIS OF $\text{Bi}_2\text{Te}_3$ QUANTUM DOTS BY PULSED LASER ABLATION IN LIQUIDS. RAJENDRA SUBEDI AND GRÉGORY GUISEBIERS**

Department of Physics and Astronomy, University of Arkansas at Little Rock, Arkansas 72204

Bismuth Telluride ( $\text{Bi}_2\text{Te}_3$ ) is an important thermoelectric material and topological insulator. In this project,  $\text{Bi}_2\text{Te}_3$  quantum dots (QDs) were synthesized for the very first time by Pulsed Laser Ablation in Liquids (PLAL) using a bottom-up synthesis protocol. Acetone was used as a solvent and the repetition rate was fixed at 1 kHz. The size and the energy band gap of  $\text{Bi}_2\text{Te}_3$  QDs were determined to be around  $\sim 12$  nm and  $\sim 1.86$  eV respectively. The quantum confinement of those  $\text{Bi}_2\text{Te}_3$  nanoparticles was confirmed by Transmission Electron Microscopy (TEM) and Raman spectroscopy.

## **THE EFFECT OF ALUMINUM SUBSTITUTION RATIO WITHIN NICKEL HYDROXIDE ON STRUCTURE AND ELECTROCHEMICAL PROPERTIES OF CATHODES FOR NICKEL-ZINC BATTERIES. JARET A. MANLEY<sup>1</sup>, SAMUEL W. KIMMEL<sup>1,2</sup>, CHRISTOPHER P. RHODES<sup>1,2</sup>.**

<sup>1</sup>Department of Chemistry and Biochemistry, Texas State University, San Marcos, TX 78666, USA, <sup>2</sup>Materials Science, Engineering, and Commercialization Program, Texas State University, San Marcos, TX 78666, USA.

Batteries that are safe, have lower cost, and have high energy density are needed for applications that range from electric vehicles to portable devices. Lithium-ion batteries are the industry standard; however, their inherent fire risks and high costs are on-going issues. Nickel-zinc batteries provide a safer alternative due to the usage of an aqueous electrolyte solution that prevents thermal runaway from occurring. The current commercially available nickel cathodes utilize a  $\beta$ -phase nickel hydroxide, which has a theoretical discharge capacity of  $289 \text{ mAh g}^{-1}$ . In contrast,  $\alpha\text{-Ni(OH)}_2$  exhibits a higher theoretical discharge capacity of  $487 \text{ mAh g}^{-1}$ , and aluminum substitution within  $\alpha\text{-Ni(OH)}_2$  results in higher capacities and improved stability in alkaline electrolyte. We evaluated the effects of different Al substitution ratios within  $\alpha\text{-Ni(OH)}_2$  on the structure and electrochemical performance. By implementing a microwave-assisted hydrothermal method, we determined that Al substituted-nickel hydroxide can be directly grown onto an electrically conductive carbon nanofiber network, and the concentration of aluminum alters the growth of the material on the carbon nanofibers. We used Scanning Electron Microscopy (SEM) to evaluate the effect of Al concentration on morphology, and we used Energy Dispersive Spectroscopy (EDS) to determine elemental composition. Atomic absorption measurements were obtained to determine the mass of

the active nickel hydroxide within the composite cathode. The different Al substitution ratios within  $\alpha\text{-Ni(OH)}_2$  resulted in different morphologies and mass loadings, which influenced the electrochemical performance. Our electrochemical testing shows that the Al substitution ratio significantly affects the electrochemical performance of cathodes. Using a lower Al substitution ratio resulted in improved retention of discharge capacity, and a higher Al substitution ratio resulted in a higher degree of capacity fade upon cycling.

## **NANOWIRE MANIPULATION IN SEM: THEORY AND PRACTICE USING SINGLE PROBE FOR NANO PRECISION ENGINEERING. UJJWAL DHAKAL<sup>1</sup>, D.C. BINOD<sup>2</sup>, RAJENDRA RAI<sup>1</sup>, YOICHI MIYAHARA<sup>1,2</sup>**

<sup>1</sup>Department of Physics, Texas State University, San Marcos, TX 78666; <sup>2</sup>College of Science and Engineering, Material Science, Engineering and Commercialization Program, Texas State University, San Marcos, TX 78666

Coupled multiple quantum dots (QDs) have been attracting significant attention because of their use in quantum information processing. To fabricate coupled QD devices, we use semiconductor nanowires (NWs) which contain QDs inside. The nanowires typically exhibit diameters ranging from 30 to 60 nm and lengths spanning from 1 to 3  $\mu\text{m}$ . To conduct a comprehensive characterization of these nanowires and fabricate the devices, it is imperative to transfer the NWs from the substrate on which they are grown (growth substrate) onto another substrate on which the devices are fabricated (device substrate). In the scanning electron microscope (SEM), a growth substrate and a device substrate are mounted to the same sample holder. To enhance the control in characterizing and testing nanowires, we used a sharp probe having a tip radius of 0.5  $\mu\text{m}$  with taper angle of 8-10 degree for the NW transfer. Challenges arise during the transfer process due to the substantial size difference between the probe and the nanowires.

We applied a negative bias voltage of 5V to the probe for transferring these vertically grown nanowires as shown in Figure 1. The process involves initially detaching them from the growth substrate and then lifting them using a probe tip. Breaking nanowires using the electrostatic force is a delicate process because when dealing with highly flexible NWs, they tend to jump away due to accumulated elastic energy at the breaking point. To address this, the nanowires are carefully broken near their bases. This is accomplished by gradually bringing the probe tip into contact with the base of a NW, and upon contact, gently applying a force by pushing the NW until the wire breaks.

To release the nanowire, the probe tip is slowly positioned above the device substrate. Once the contact is detected between the NW and the device substrate, a positive bias voltage of 10V is applied to the probe tip. When the nanowire is held only at one of its ends, it

promptly responds to the attractive van der Waals forces emanating from the substrate and the NW is released from the probe as shown in Figure 2. We will present more details of the NW transfer process and the features of the transferred NWs by atomic force microscopy and Kelvin probe force microscopy techniques.



Figure 1. SEM image of vertically grown nanowire.

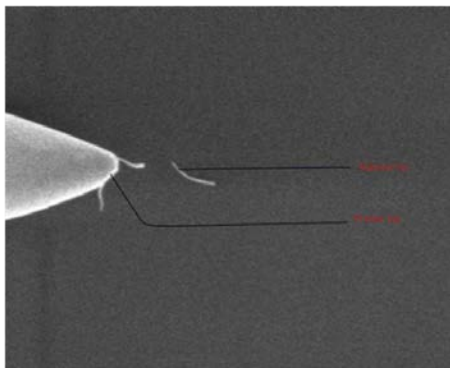


Figure 2. SEM image of transferred nanowires.

**WEATHERING EFFECTS ON POLYMERIC AZOBENZENE EXAMINED BY ATOMIC FORCE MICROSCOPY.** SCOTT BARRETT, WILLIAM J. BRITTAIN, KEISUKE IKEHATA  
Ingram School of Engineering, Texas State University, San Marcos, Texas 78666

The application of chemicals to increase efficiency in renewable energy has been of interest for the scientific community as we transition into the new era of technology. As scientists continue to develop new chemicals, many are not analyzed for their environmental impacts. For example, azobenzene is a chemical that has been applied to material science and was traditionally used as a dye for consumer goods. Unfortunately, when azobenzene was used as a dye by German painters, it would be inhaled and lead to bladder tumors as well as other cancers. This danger from a commonly used chemical should be reviewed for implementation into renewable energy to reduce potential danger to the water, soil, and air. Azobenzene has been reviewed in this study to understand the toxicity towards humans, animals, fish, and the environment.

Azobenzene has the ability to store energy from photoexcitation, transitioning from the trans state to the cis state via sunlight. When azobenzene is in the cis state, it may relax back to the trans state in time or under visible light; thus, azobenzene may store energy. This storage obtained through photoexcitation can be applied within heat storage or into organic photovoltaics to increase efficiency. However, if the derivative of azobenzene has high aqueous solubility, leakage may occur and subsequently pollute the environment. To create a model for this system, a polycarbonate thin-film azobenzene was produced. The azobenzene thin-film was placed on the roof of the Chemistry building at Texas State University for a month to test the weathering effects from rain, wind, and heat exposure.

The thin-film was tested by the following techniques to assess weathering: atomic force microscopy, UV-Vis spectroscopy, and infrared spectroscopy. Atomic force microscopy is used to create a two-dimensional topography of the film and to identify artifacts at the atomic level as seen in Figure 1. UV-Vis spectroscopy is used to analyze the concentration of the sample. Infrared spectroscopy is used to identify compounds in the sample. The atomic force microscopy data shows substantial defects including ridges and hills within the thin-film. UV-Vis spectroscopy found 19.7% leakage of azobenzene from the film. Infrared spectroscopy showed a large water peak, indicating the film had absorbed water from rain.

Utilization of organic compounds in renewable energy must be researched carefully to understand the environmental implications. The modeling of compounds within polymers or similar systems to solar panels is important to study the effects of organic photovoltaics in outdoor conditions. Limitations of coating the organic photovoltaics with a sealant may reduce efficiency which lowers the profit margin for electricity production. The future relies on renewable energy to not only produce sustainable energy but also to save the planet.

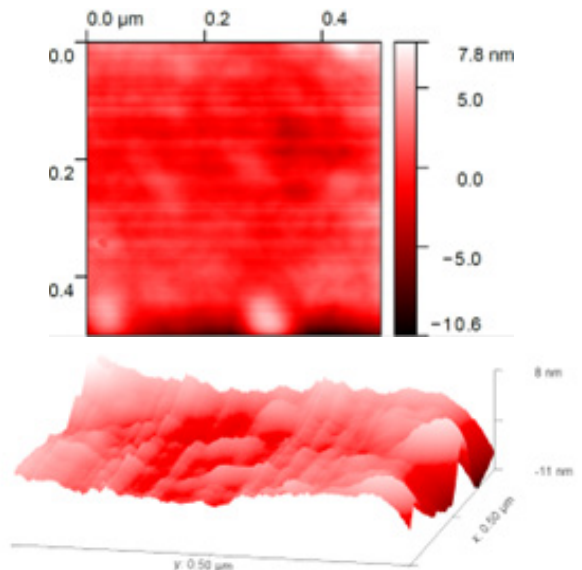
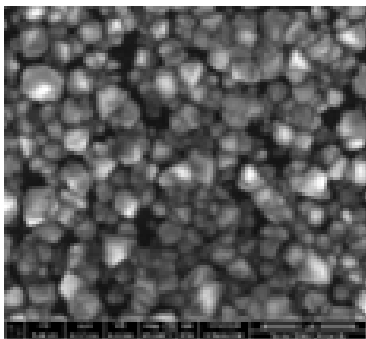


Figure 1. Atomic Force Microscopy of Polymeric Azobenzene

**OPTIMIZATION OF HFCVD DIAMOND GROWTH PARAMETERS USING BAYESIAN ALGORITHM: INSIGHTS FROM SEM IMAGING.** RON SAHA<sup>1</sup>, MARIA SULTANA<sup>2</sup>, ARIFUL HAQUE<sup>2</sup>.

<sup>1</sup>Materials Science, Engineering, and Commercialization, Department of Electrical Engineering, Texas State University, San Marcos, TX 78666; <sup>2</sup>Electrical Engineering, Ingram School of Engineering, Texas State University, San Marcos, TX 78666

This study explores the optimization of diamond growth parameters using the hot filament chemical vapor deposition *via* machine learning based on a closed-loop Bayesian optimization algorithm, which marks a breakthrough in precisely identifying the optimal conditions for diamond synthesis. This algorithm, contrasting traditional trial-and-error, uses iterative learning to refine the diamond growth parameters, leading to a significant improvement in the quality of diamond films. For our Bayesian model, deposition time, growth temperature, flow rate ratio of CH<sub>4</sub>/H<sub>2</sub> gas, and distance between the film and the Tungsten wires have been used as input parameters. For characterization of the diamond, scanning electron microscopic images were compared to study the morphology of the diamond crystal structure. The SEM image in Figure 1 shows the best diamond film with well-faceted structure and an average grain size of ~0.2 μm with growth condition (T~700 °C, P-20 Torr, CH<sub>4</sub>/H<sub>2</sub> flow ratio of 1/49, substrate to filament distance 7 mm). Figure 2 shows a comparatively low-quality film having a high concentration of sp<sup>2</sup> carbon content with a change of flow rate ratio of CH<sub>4</sub>/H<sub>2</sub> to 3/47. For CH<sub>4</sub> concentration of 1% vol. depicted in Figure 1, triangular (111) planes are predominant, and a continuous film is obtained, whereas concentration of 3% vol. have ballas-like shape and no continuous film is obtained. For substrate temperature variation, best diamond film is grown around 700 °C having dominant triangular (111) faces. Moreover, even in the best quality diamond as shown in Figure 1, blank spots can be seen among the diamond facets, for which non uniform nano-diamond seeding might be responsible. Raman analysis also supports the relative morphological information about the quality of diamond films.



**Figure 1:** SEM image of diamond film grown with 1% vol. CH<sub>4</sub> having 0.2μm average grain size.

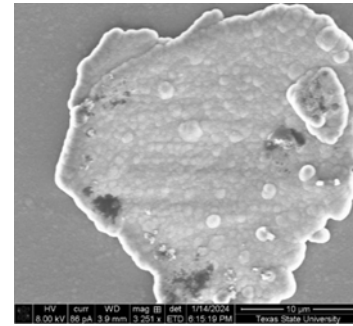


**Figure 2:** Low magnification SEM image of diamond film grown with 3% vol. CH<sub>4</sub> having ballas shape.

**OBSERVATION OF SINGLE-ELECTRON TUNNELING IN GOLD NANOPARTICLE - DNA - GOLD JUNCTION BY ELECTROSTATIC FORCE MICROSCOPY.** RIGO LUNA<sup>1</sup>, DAMILOLA RUNSEWE<sup>1</sup>, NOAH AUSTIN-BINGAMON<sup>1</sup>, BINOD D.C.<sup>1</sup>, TANIA BETANCOURT<sup>1,2</sup>, YOICHI MIYAHARA<sup>1,3</sup>

<sup>1</sup>Material Science, Engineering, and Commercialization program, Texas State University, San Marcos, Texas, 78666; <sup>2</sup>Department of Chemistry and Biochemistry, Texas State University, San Marcos, Texas 78666; <sup>3</sup>Department of Physics, Texas State University, 601 University Dr, San Marcos, Texas, 78666

Molecular nano electronics will soon be emerging as potential successors to modern day silicon chips due to the inherent limitations of modern-day lithographic methods. As a result, various molecules are currently being studied as potential candidates and building blocks for said nanoelectronic devices. Due to its programmable nature, rapid production, and potential for charge transfer, DNA has gained wide interest as a promising new material in the ever-growing field of molecular nano-electronics. In this research, we explore and probe the use of DNA molecules as charge transfer mediums via mechanical charge-sensing by Atomic Force Microscopy (AFM). For any type of DNA nano-electronic device to be of practical use, a thorough understanding of the electrical properties of the charge-transfer in the DNA molecules is required. Attempts at characterizing the electrical properties of individual DNA molecules have previously been performed; however, there still remains disagreement within the scientific community regarding the classification of DNA molecules as an electronic material. Much of this disagreement has been the result of varying methodologies as well as potential contact and deformation of the DNA molecule being probed (Hippes, 2001).

To remedy such issues, a standard, non-invasive, and repeatable method is required to characterize DNA molecules and their charge-transfer capabilities. In this research, we attempt to provide such a method and characterize individual hybridized DNA molecules attached to gold via thiol linkers using a mechanical

non-contact method that allows for the measurement and observation of single-electron charging events within target molecules *via* the use of AFM. Silicon-Gold substrates are prepared, on which DNA Self Assembled Monolayers are grown and later hybridized with Gold NP functionalized complementary DNA. The charge transfer through the individual DNA is then measured by Electrostatic Force Microscopy at cryogenic temperatures. To induce single-electron charging, metal coated cantilever tips are biased, oscillated, and brought close to the attached gold nanoparticles. By oscillating the tip, the quantized charging energy within the nanoparticle is also oscillated. If the amplitude of cantilever oscillation is tuned properly, a single electron can be controlled and is allowed to overcome the charging coulomb blockade, allowing charge transfer through the DNA. Due to the coulombic force from a moving charge, the cantilever is able to sense the charge transfer and *via* the oscillating feedback loop, the charging event can be observed. The methods and theory have been adapted from Miyahara et al, 2017. Once charging events have been observed, the cantilever can be used to also probe the various charging levels in the molecule-particle system, allowing for charging spectra to be obtained. The spectra obtained may then be used to quantify the charge transfer properties of DNA molecules. To help distinguish and identify charging events within the target DNA, topographical images are taken and supplemented with energy-dissipation images as well. As the tip scans, the back-force from the charging will change the energy loss and gain in oscillation. This energy loss can be measured and quantified, allowing for the imaging of charging across the surface. Due to the symmetric and position dependent nature of the electric potential from the tip, charging events manifest themselves in the form of rings as seen in Figure 1.

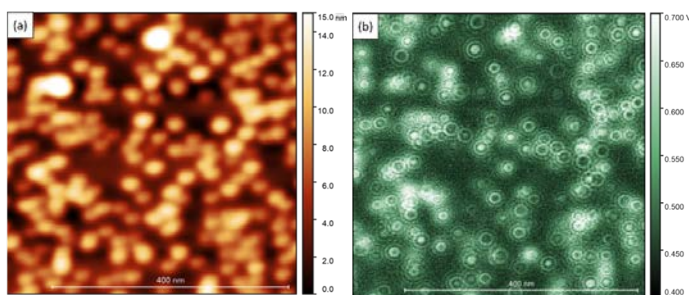


**Figure 1.** DNA-Nanoparticle sample imaged via AFM. (a) Depicts sample topography. (b) Depicts charge transfer charging rings

#### References:

- K. W. Hipps. It's All About Contacts. *Science*, 2001, 294(5542):536–537.
- Miyahara, Y., Roy-Gobeil, A., Grutter, P. Quantum state readout of individual quantum dots by electrostatic force detection. *Nanotechnology*, 2017, 28(6):064001.

## DIAMOND GROWTH ON $\beta$ -GALLIUM OXIDE ( $\beta$ -Ga<sub>2</sub>O<sub>3</sub>) USING ALUMINUM NITRIDE (AlN) INTERLAYER FOR THERMAL MANAGEMENT. MARIA SULTANA<sup>1</sup> AND ARIFUL HAQUE<sup>1,2</sup>

<sup>1</sup>Electrical Engineering, Ingram School of Engineering, Texas State University, San Marcos, TX 78666

<sup>2</sup>Materials Science, Engineering & Commercialization Program, Texas State University, San Marcos, TX 78666

Owing to its exceptional properties like ultrawide bandgap (UWBG) of 4.9 eV, and remarkably high critical field strength of 8 MV/cm,  $\beta$ -Ga<sub>2</sub>O<sub>3</sub> is highly suitable for high-power high-frequency electronics and solar-blind photodetectors which are exceedingly in-demand nowadays. Furthermore, the availability of large-area native  $\beta$ -Ga<sub>2</sub>O<sub>3</sub> substrates from melt-grown techniques has made it the most suitable UWBG semiconductor for next-generation electronic devices. However, its very low thermal conductivity of only 27 W/m-K is thwarting its implementation in actual applications. Due to the low thermal conductivity, thermal hot spots are created inside  $\beta$ -Ga<sub>2</sub>O<sub>3</sub> when applied in power devices and thus the electronic conduction is critically hampered, leading to mediocre performance of  $\beta$ -Ga<sub>2</sub>O<sub>3</sub>-based devices. Hence, the heat dissipation from  $\beta$ -Ga<sub>2</sub>O<sub>3</sub> has become a crying need. Diamond, with the highest thermal conductivity known to date (2200 W/m-K), is exceptional in working as a heat spreader. Therefore, a diamond thin film on the  $\beta$ -Ga<sub>2</sub>O<sub>3</sub> will work as a good heat sink mitigating the heating issue of  $\beta$ -Ga<sub>2</sub>O<sub>3</sub> devices. However, many endeavors regarding diamond incorporation on  $\beta$ -Ga<sub>2</sub>O<sub>3</sub> didn't produce viable diamond/ $\beta$ -Ga<sub>2</sub>O<sub>3</sub> heterojunction due to multiple shortcomings like usage of expensive diamond and  $\beta$ -Ga<sub>2</sub>O<sub>3</sub> substrates, diamond film delamination due to thermal expansion mismatch, and decomposition of  $\beta$ -Ga<sub>2</sub>O<sub>3</sub> in the highly reactive hydrogen (H<sub>2</sub>) -rich environment required for diamond growth. Later, the issue of being pricey was solved by growing the diamond using the chemical vapor deposition (CVD) technique on  $\beta$ -Ga<sub>2</sub>O<sub>3</sub> thin films rather than the expensive substrates used earlier, and the  $\beta$ -Ga<sub>2</sub>O<sub>3</sub> delamination and decomposition issues were mitigated by using a SiO<sub>2</sub> interlayer. However, SiO<sub>2</sub> itself having even lower thermal conductivity (1.3 W/m-K) than  $\beta$ -Ga<sub>2</sub>O<sub>3</sub> when used as an interlayer hampers the thermal propagation from  $\beta$ -Ga<sub>2</sub>O<sub>3</sub> to diamond resulting in degradation of diamond heat sink performance. In the pursuit of solving this, we used AlN grown using the atomic layer deposition technique, as an interlayer between CVD diamond and  $\beta$ -Ga<sub>2</sub>O<sub>3</sub> thin films which not only protects the  $\beta$ -Ga<sub>2</sub>O<sub>3</sub> from H<sub>2</sub> decomposition owing to its non-reactive nature in a reactive H<sub>2</sub> environment but also aids in thermal propagation towards diamond due to having a moderately large thermal conductivity of 321 W/m-K. The surface morphology of as-grown diamonds was studied using scanning electron microscopy (SEM).

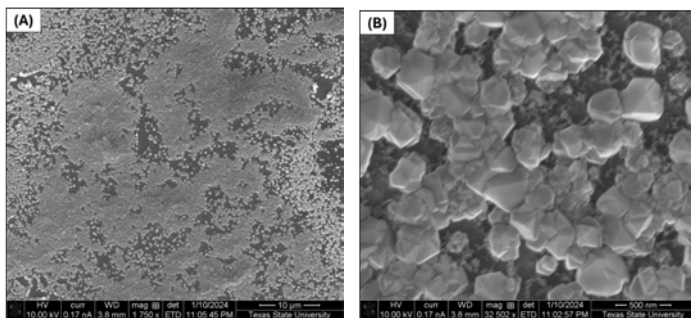


**Figure 1.** A) Large area diamond grown on  $\beta$ -Ga<sub>2</sub>O<sub>3</sub> using AlN interlayer; B) High-magnification image of as-grown diamond showing well-defined (111) facets.

The SEM image depicted in Figure 1A shows long-range large-area, good coverage growth of diamond on  $\beta$ -Ga<sub>2</sub>O<sub>3</sub> without any delamination. Also, a high magnification image of the as-grown diamond illustrated in Figure 1B shows well-defined (111) facets and quite large grain sizes (~300 nm) indicating good quality of diamonds and thus shows great promise for good heat spreading utilizing the diamond layer. The reason behind the presence of uncovered regions on the  $\beta$ -Ga<sub>2</sub>O<sub>3</sub> film observed in both SEM images was attributed to the non-uniformity of nano-diamond seeding on AlN required for diamond nucleation.

#### ANGLE-RESOLVED X-RAY PHOTOELECTRON SPECTROSCOPY OF SPIN-CASTED TRIPLE HALIDE PEROVSKITE. MD MAHAMUDUJJAMAN<sup>1</sup>, LUISA M SCOLFARO<sup>1,2</sup>, WILHELMUS J. GEERTS<sup>1,2</sup>

<sup>1</sup>Materials Science Engineering and Commercialization, Texas State University, San Marcos, TX 78666  
<sup>2</sup>Department of Physics, Texas State University, San Marcos, TX 78666.

Perovskite materials have attracted the scientific community's attention due to their photovoltaic properties and their low manufacturing cost. Films can be deposited with near-room temperature (RT) solvent-based techniques including spin-casting, blade-coating, slot-die printing, and inkjet printing. Triple halide perovskites exhibit an adjustable wide bandgap, offering potential applications in tandem solar cells when combined with silicon bottom cells. Despite such improvement in efficiencies and lower manufacturing costs, perovskite solar cells could not be a marketable product without improving device stability. Here, we studied angle-resolved X-ray photoelectron spectroscopy (XPS) of spin-coated (Cs<sub>0.22</sub>FA<sub>0.78</sub>)Pb(I<sub>0.85</sub>Br<sub>0.15</sub>)<sub>3</sub> + 3 mol % MAPbCl<sub>3</sub> absorber layer. This triple halide is also denoted by Cs<sub>22</sub>Br<sub>15</sub>. DMF-based inks were prepared in a glovebox and spin casted on plasma cleaned glass/ito substrates (Khakurel et al., 2024). The wet films were annealed for 30 minutes at 100°C. The phase of the annealed and unannealed perovskite samples were

analyzed by XRD measurement. The results show that the annealed samples have a photo-active  $\alpha$  phase while the unannealed perovskite samples possess a photo-inactive  $\delta$  phase. The chemical composition of the surface of the perovskite films was studied by angle-resolved XPS. ARXPS is a good technique to study the photochemical and thermal decomposition of perovskite solar cell. Samples were cleaned with an ion/cluster beam prior to XPS measurements. A low energy beam was used to avoid damaging the perovskite layer. The survey spectrum of freshly made glass/perovskite sample shows the characteristic peaks of perovskite crystals such as Pb4f, Br3d, I3d, Cs3d, C1s as shown in Figure 1. If we zoom in between 283 eV and 287 eV, there is a peak at ~286 eV and a secondary peak at ~284 eV which represent C-N bond and C-C bond respectively.

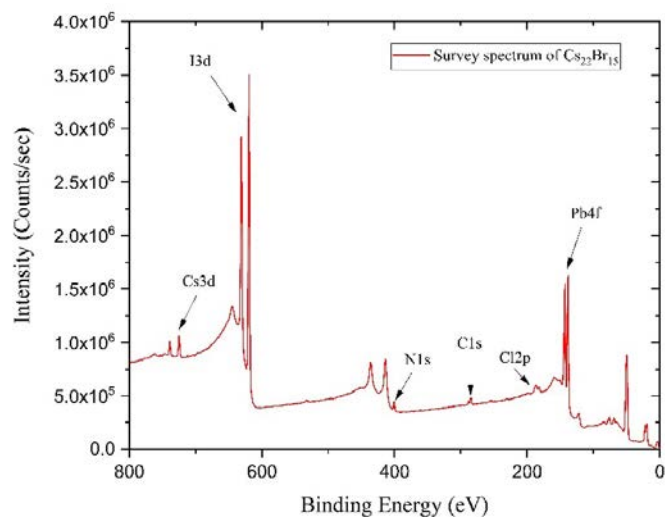


**Figure 1.** The survey spectrum of freshly made glass/perovskite sample (raw data)

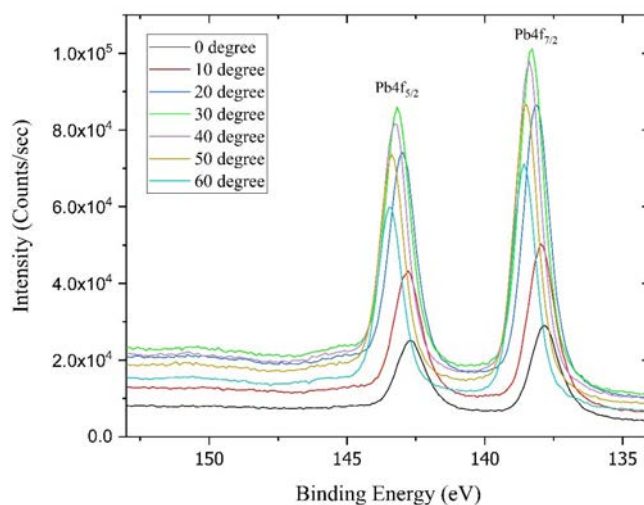


**Figure 2.** XPS spectra of Pb at different angles

Figure 2 shows the elemental XPS data of Pb at different angles. At the angle of 30 degrees, the counts/sec become maximum which suggest that the amount of

Pb is higher at bulk than at the surface of the sample. We also study the effect of heat and moisture on the triple halide perovskite and will present the results in the final presentation. To the best of our knowledge, no one reported the XPS study on Cs<sub>22</sub>Br<sub>15</sub> before.

#### References:

Khakurel, N., Amyx, D., Miyahara, Y., Geerts, W. Slotdie coating of Formamidinium-Cesium mixed halide perovskites in ambient conditions with FAc additive. 2024, *in press, MRS Communications*.

#### Acknowledgment:

Part of this work is supported by a TxState Research Enhancement grant. We acknowledge help of the shared research operations group of TxState with the XPS measurements.

### EVALUATION OF STRUCTURE AND PROPERTIES OF IRIIDIUM-TITANIUM OXIDES SYNTHESIZED USING HIGH ENERGY BALL MILLING. KEEGAN BAILEY<sup>1</sup>, JESUS ADAME SOLORIO,<sup>1</sup> CHRISTOPHER RHODES<sup>1,2</sup>

<sup>1</sup>Department of Chemistry and Biochemistry, Texas State University, San Marcos, TX, and <sup>2</sup>Materials Science, Engineering, and Commercialization Program, Texas State University, San Marcos, TX.

Electrochemical splitting of water generates hydrogen from water and can be powered by renewable energy sources. Iridium oxide (Ir<sub>2</sub>O<sub>3</sub>) which is currently used as an Oxygen Evolution Reaction (OER) electrocatalyst is extremely expensive and has global supply issues. The introduction of titanium into Ir<sub>2</sub>O<sub>3</sub> provides a method to reduce cost and maintain or improve stability while minimizing loss of activity. High energy ball milling provides a highly scalable method to synthesize mixed metal oxides. We investigated the synthesis of Ir<sub>1-x</sub>Ti<sub>x</sub>O<sub>2</sub> (x = 0, 0.4, 0.5, 0.6) using High-Energy Ball Milling (HEBM), the post-synthesis thermal treatment, and we subsequently evaluated the structure and electrochemical performance of the materials as oxygen evolution electrocatalysts. In addition to different Ir:Ti ratios, we determined the effect of ball milling time on the structure of the materials. Characterization of the synthesized catalysts using X-ray diffraction showed peak shifts consistent with a rutile phase containing both Ir and Ti. Porosimetry analysis shows that when compared to the starting Ir<sub>2</sub>O<sub>3</sub> materials, the synthesized catalysts exhibit both higher surface area and increased porosity, both of which are factors in catalytic activity. Scanning electron microscopy (SEM) and energy dispersive spectroscopy (EDS) were performed to investigate the morphology and elemental composition of the catalysts. The morphologies of the synthesized catalysts were similar, each exhibiting large aggregates composed of smaller nanoparticles of roughly a few hundred nanometers in

size (Figure 1). Analysis with EDS shows that iridium and titanium are evenly dispersed throughout the sample. Electrochemical analysis shows the iridium-titanium oxide catalysts synthesized using high energy ball milling function as OER catalysts and exhibit good OER activity and electrochemical stability.

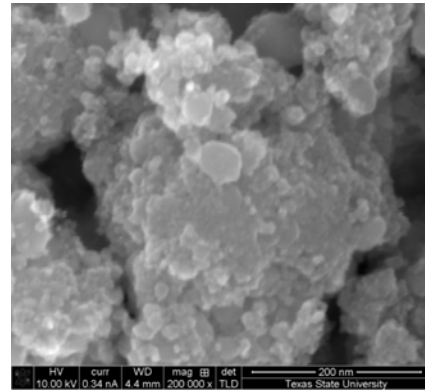


**Figure 1.** Scanning electron microscopy (SEM) image of Ir<sub>0.5</sub>Ti<sub>0.5</sub>O<sub>2</sub> prepared using high-energy ball milling.

### INNOVATIVE GROWTH AND PROCESSING STRATEGIES TO OPTIMIZE STRUCTURAL PROPERTIES OF GAN BUFFER LAYER IN GAN/ALGAN HEMTS. ISTIAQ FIROZ SHIAM AND ARIFUL HAQUE

Ingram School of Engineering, Texas State University, San Marcos, Texas 78666.

In recent years, GaN has gathered significant attention within the wide bandgap semiconductor community, thanks to its compatibility in optoelectronics, high-power semiconductor devices, and as a compelling alternative to traditional silicon-based technologies. Despite its favorable attributes, in GaN-based AlGaN/GaN HEMTs, GaN poses challenges in terms of dislocation density and growth rate mismatch during its multilayer fabrication processes for epitaxial growth. While researchers have strived to optimize layer composition, thickness, and growth conditions, there remains an underexplored realm concerning the correlation between GaN growth rates, thermal treatment, and dislocations, with implications for device performance. This study utilized two distinct approaches to enhance the structural properties of GaN in AlGaN/GaN HEMTs. The first involves a multi-graded/skewed growth method for AlGaN/GaN HEMT on a Si (111) substrate, utilizing MOCVD to vary the growth rate during GaN layer deposition. This innovative approach aims to improve interlayer structure and reduce dislocations. The second approach explores the impact of nanosecond pulsed laser annealing (PLA) on both structural and electrical attributes, emphasizing the meticulous adjustment of annealing conditions to minimize the dislocation density of the GaN layer. The layer-by-layer growth of HEMTs was monitored by Scanning Electron Microscopy (SEM) to gain insights

into the layer thickness, crucial for calculating the GaN deposition rate (Figure 1). X-ray diffraction (XRD) was employed to quantify the dislocation density, revealing 1.25 times (from  $7.07 \times 10^8/\text{cm}^2$  to  $5.7 \times 10^8/\text{cm}^2$ ) improvement in the GaN buffer layer under a specific PLA condition. Subsequent analysis of the dislocation profile within the GaN layer will be conducted using the Transmission Electron Microscopy (TEM). Hall measurements were employed to assess the carrier concentration and mobility within the two-dimensional electron gas ( $^2\text{DEG}$ ) channel of HEMT. The obtained data revealed a carrier concentration of  $1.279 \times 10^{13}/\text{cm}^2$  and a mobility of  $1180 \text{ cm}^2/\text{V}\cdot\text{s}$ , providing valuable insights into the electronic properties of the HEMT device.

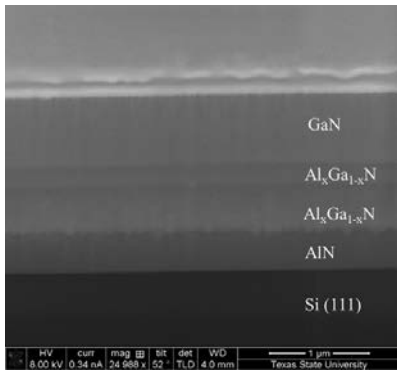


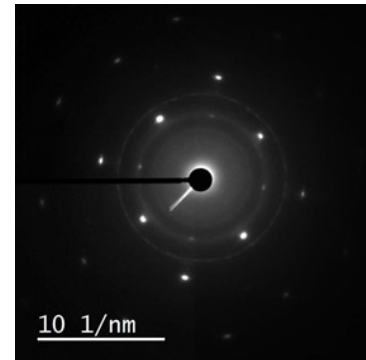
**Figure 1.** Layer-by-layer deposition of AlGaIn/GaN HEMT observed by Scanning Electron Microscopy (SEM).

### SYNTHESIS AND MICROSTRUCTURAL ANALYSIS OF FeCoNiCuSi HIGH ENTROPY ALLOY. R.A. SHOHAN, A. PONCE.

Department of Physics and Astronomy, University of Texas at San Antonio, San Antonio, Texas 78249

High Entropy Alloys (HEAs) constitute an unconventional class of metallic materials, characterized by their distinctive composition featuring at least four or more primary elements in nearly equimolar proportions. This unique composition results in remarkable mechanical, thermal, and magnetic properties compared to traditional alloys. Herein, an equiatomic solid mixture of 99.99% (wt%) pure metals of Fe, Co, Ni, Cu and Si have been used for the synthesis of high entropy alloy deposited directly on pure sodium chloride crystal substrate by employing the thermal evaporation technique under high vacuum. Morphological, microstructural, and phase compositional analysis of the synthesized alloy have been performed by analytical high-resolution methods: scanning and transmission electron microscopy. Transmission electron microscopy (TEM) studies with selected area diffraction have been conducted to comprehensively characterize their structure and enhance our understanding of their origin. As well as elemental analysis was performed using high resolution TEM energy dispersive X-ray spectroscopy

(EDS). From the analysis, the synthesis of thin films has been revealed to be polycrystalline with different grain size, cubic crystal structure with lattice parameter  $a = 0.356 \text{ nm}$  which is in the range of  $0.35 \text{ nm} - 0.36 \text{ nm}$ , and almost same percentage of each chemical component are present in the deposited films.



### LASER ANNEALING INDUCED GROWTH AND CHARACTERIZATION OF CARBON NANOSTRUCTURES. SAIF TAQY<sup>1</sup>, PALLAB SARKAR<sup>1</sup>, ARIFUL HAQUE<sup>1,2</sup>,

<sup>1</sup>Materials Science, Engineering, and Commercialization (MSEC); <sup>2</sup>Electrical Engineering, Ingram School of Engineering, Texas State University, San Marcos, TX 78666, USA.

Quenched carbon (Q-carbon) is a recently discovered carbon allotrope that exists as a non-equilibrium, metastable phase of carbon. Q-carbon is distinguished by its distinctive dense structure consisting of diamond tetrahedra that have central atoms placed in a random manner. Additionally, nanodiamonds (NDs) are a novel kind of carbon nanomaterials that have attracted interest due to their unique properties, including low toxicity, long-lasting fluorescence, simplicity of modification, inherent compatibility with biological systems, and other fundamental traits of bulk diamonds. This study employs pulsed laser deposition (PLD) for developing thin films of diamond-like carbon (DLC), followed by consecutive pulsed laser annealing (PLA) to create various carbon forms, including nano-diamond and Q-carbon on different substrates such as  $\text{Al}_2\text{O}_3$ ,  $\text{Ga}_2\text{O}_3$ , GaN, and AlN. Through the use of laser-solid melt interaction models, undercooling is achieved by ultrafast melting and quenching of molten material, resulting in the creation of composites consisting of Q-carbon and nanodiamond. The SEM images reveal filamentary or cellular Q-carbon structures (Figure 1a), where the top graphitic flake-like layer is covered in amorphous  $\alpha$ -carbon. To further characterize the Q-carbon film, the top graphitic layer is etched by utilizing an argon polisher, and the resultant film demonstrates filaments reaching the Q-carbon layer (Figure 1b). The high-resolution TEM image demonstrates the thickness of the Q-carbon

layer to be around 50 nm, which is further supported by the simulation of laser interaction with materials (Figure 1c). By carefully optimizing the laser annealing parameters, nanodiamonds were formed, particularly near the filaments of Q-carbon, as they provided sufficient nucleation sites for the nanodiamond generation (Figure 1d-f). The nanodiamonds' Raman spectra display a wide peak at 1320  $\text{cm}^{-1}$ , accompanied by a red shift of around 12  $\text{cm}^{-1}$  due to phonon confinement. In this study, a critical shortcoming of Q-carbon formation, the limitation of suitable substrates, has been overcome. We have been successful in fabricating Q-carbon on high thermally conductive substrates, such as GaN and AlN for application in high-power semiconductor devices. Furthermore, the fabrication of Q-carbon on wide bandgap semiconductors opened up a pathway for direct diamond integration with these materials, thereby removing the necessity for a non-carbon interfacial layer for subsequent diamond growth. The cross-sectional SEM image in Figure 1g and the EDS scanning spectra in Figure 1h demonstrate the growth of Q-carbon on

GaN, thereby presenting a proof of concept for the incorporation of Q-carbon into future electronic devices. Ultimately, this research enhances the applicability of Q-carbon and proceeds further from the conventional  $\text{Al}_2\text{O}_3$  substrates with a primary focus on the next generation of electronic device applications. This would allow the creation of advanced high-power devices that incorporate diamond-thin films with different materials. Furthermore, the direct formation of nanodiamonds from DLC films by inducing laser annealing provides a simple and efficient method for nanodiamond growth and characterization, which can overcome certain limitations of the conventional deposition processes and assist in increasing the suitability of nanodiamonds to be utilized in different applications and also can be useful for further research into this field. Moreover, the results obtained from this research will also be crucial in expanding the feasibility of Q-carbon to be utilized in numerous real-life applications, such as supercapacitors, electron field-emission devices, novel interlayers for subsequent material growth, etc.

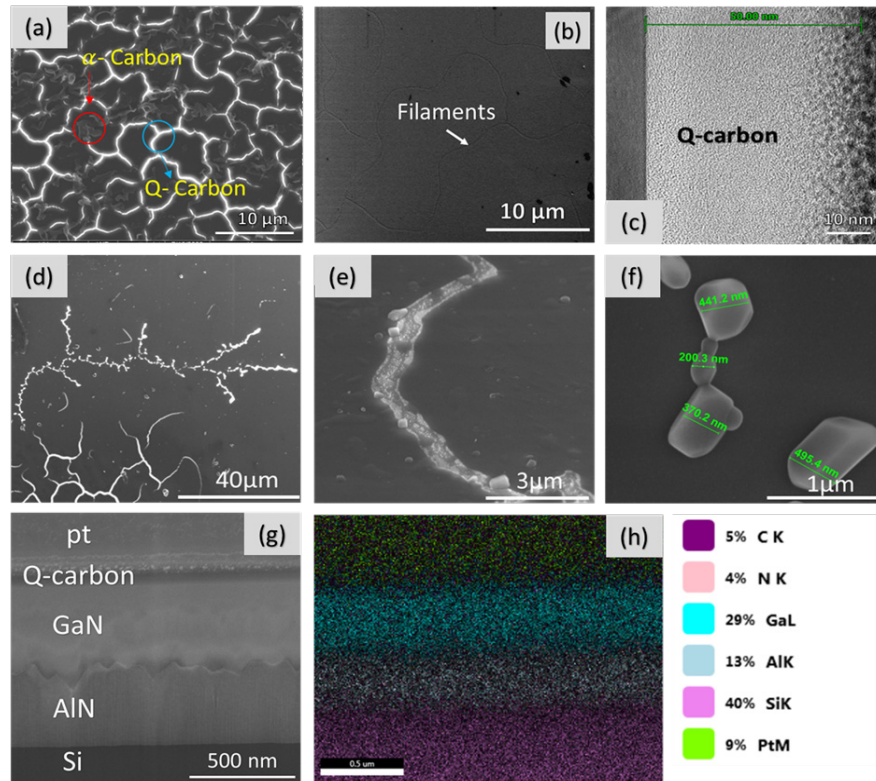


**Figure 1:** SEM images of (a) filamentary structure of Q-carbon with the top  $\alpha$ -carbon layer on  $\beta$ - $\text{Ga}_2\text{O}_3$ , (b) Q-carbon filaments after etching of  $\alpha$ -carbon on  $\text{Al}_2\text{O}_3$ , (c) HRTEM image of Q-carbon on  $\text{Al}_2\text{O}_3$ ; (d, e, and f) SEM images of nanodiamond formation on the Q-carbon filament region; (g) cross-sectional SEM image of Q-carbon grown on GaN, and (h) EDS scan of Q-carbon on GaN.

**EFFECT OF ANNEALING ON ELECTRICAL PROPERTY OF PLATINUM NANOWIRES DEPOSITED BY FOCUSED ELECTRON BEAM INDUCED DEPOSITION.** RAJENDRA RAI<sup>1</sup>, UJJWAL DHAKAL<sup>1</sup>, BINOD D.C.<sup>2</sup>, YOICHI MIYAHARA<sup>1,2</sup>.

<sup>1</sup>Physics Department, Texas State University San Marcos, 78666 Texas, United States; <sup>2</sup> Material Science, Engineering, and Commercialization program, Texas State University San Marcos, 78666 Texas, United States

A single-electron transistor (SET) is a nano electronic device that works by the quantum mechanical tunneling of single electrons. While SETs have promising applications such as ultra-low power logic circuits and qubit readout, the fabrication of SETs requires a tiny nanometer scale metallic island (a few nm diameter) to be quantum mechanically coupled to source and drain electrodes (Prima GD (2019)). The long-term goal of this project is to fabricate an SET by directly writing the required structure (island, source, and gate electrodes) with the Focused Electron-Beam Induced deposition (FEBID) of platinum on microelectrodes fabricated by lithography. However, FEBID-deposited nanoelectrodes exhibit high resistance because the deposited structures are mixed with unwanted precursor elements like carbon due to its precursor Me<sub>3</sub>CpMePt (IV), (Me: methyl, Cp: cyclopentadienyl) (Holguin Lerma (2016)). We study electrical properties of Pt nanowires deposited by FEBID technique. We performed the FEBID deposition in Scanning Electron Microscope (Helios Nano Lab 400/400S/400 ML/600). In particular, we investigated the post-deposition processing techniques to turn the deposited nanowires into electrically conducting as pure Pt metals. Huth M (2018) reported that post-processing by thermal annealing reduced the carbon content in the deposition, and that the processed nanowires resistance decreased to 10s ohm. We deposited the nanowires with different thickness ranging from 2 nm to 200 nm. The typical length of the nanowires is 1 um. Y. Fang (2014) reported that the as-deposited nanowires can be made much more conductive after annealing in pure oxygen atmosphere.

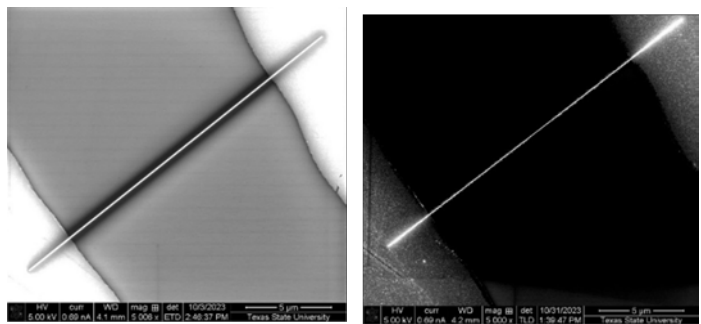


**Figure 1.** FEBID deposited nanowire on gold electrode. Left - a nanowire before annealing; Right - same nanowire after annealing.

We performed the annealing of the as-deposited nanowires at temperature 275 °C in air for 4 hours, resulting in the increase in electrical conductance by five orders of magnitude. The resistances of the nanowires are found to be around 10K ohms after the annealing. Figure 1 shows the SEM (Scanning Electron Microscope) images of the same nanowire before annealing (left) and after (right) the annealing. Figure 2 shows the topography of the nanowires after annealing measured by Atomic Force Microscope (AFM). Figure 3 shows the temperature dependence of the resistance of an annealed Pt nanowire which was measured down to 100 mK. In addition to these findings, to our surprise some nanowires are as conductive as bulk material, which is something that requires more in-depth study. We will present length and width dependence of the electrical conductivity and their correlation with the structure of the nanowires measured by AFM and Kelvin Probe Force Microscopy.

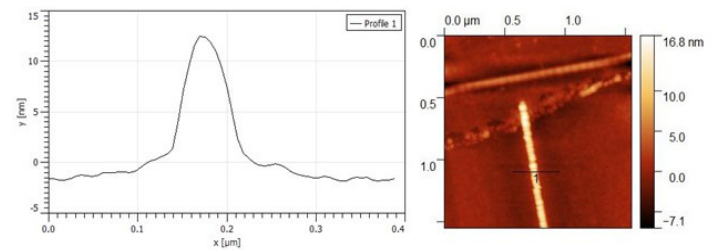


**Figure 2.** AFM topography measurement of the nanowire after annealing

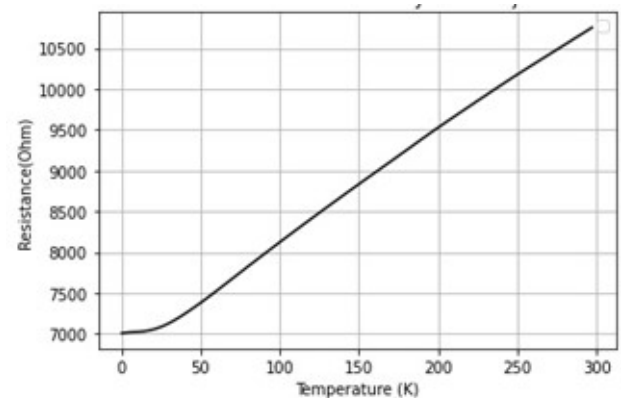


**Figure 3.** Temperature dependence of the resistance of a Pt nanowire after annealing.

**References:**

Prima, G.D., Sachser, R., Trompenaars, P., Mulders, H., Huth, M. Direct write single electron transistors by focused electron beam induced deposition. *Nano Future*. 2019, 3(2):025001.

Huth, M., Porrati, F., Dobrovolskiy, O.V. Focused electron beam induced deposition meets materials science. *Microelectron Eng*. 2018, 185- 186:9-28. doi: 10.1016/j.mee.2017.10.012

Holguin Lerma, J. A. Characterization of Deposited Platinum Contacts onto Discrete Graphene Flakes for Electrical Devices. Master thesis 2016, King Abdullah University of Science and Technology.

Fang, Y., Qin, S.Q., Zhang, X.A., Liu, D.Q., Chang, S.L.  
 Annealing effect of platinum-incorporated nanowires  
 created by focused ion/electron-beam-induced deposition.  
*Chinese Physics B* 2014, 23: 088111.

## LARGE AREA DIAMOND GROWTH ON $\beta$ -GA<sub>2</sub>O<sub>3</sub> AND AlN USING Q-CARBON INTERLAYER.

PALLAB SARKAR<sup>1</sup>, SAIF TAQY<sup>1</sup>, ARIFUL HAQUE<sup>1,2</sup>.

<sup>1</sup>Materials Science, Engineering, and Commercialization (MSEC), and <sup>2</sup>Electrical Engineering, Ingram School of Engineering, Texas State University, San Marcos, TX 78666

Ultra-wide bandgap materials, such as AlN and  $\beta$ -Ga<sub>2</sub>O<sub>3</sub>, play a crucial role in advancing high-power and high-frequency technologies. However, the low thermal conductivity of these materials poses a significant challenge for effective heat management in high-power devices. Employing diamond films for superior thermal conductivity poses challenges in depositing good quality diamonds on AlN and  $\beta$ -Ga<sub>2</sub>O<sub>3</sub> due to obstacles related to carbon solubility and surface energy. In response, we introduce a pioneering method utilizing pulsed laser

annealing (PLA) to form a quenched carbon (Q-carbon) layer on  $\beta$ -Ga<sub>2</sub>O<sub>3</sub> and AlN films. This enables the direct deposition of diamond films without the need for a non-carbon interfacial layer or nanodiamond seeding layer. Q-carbon acts as a key interlayer in low-thermal semiconducting materials, allowing for improved diamond formation without the use of dielectric interlayers. Leveraging the unique properties of Q-carbon, the film undergoes a 4-hour growth in the HFCVD chamber, taking advantage of its abundance of diamond tetrahedra for highly active surface adsorption sites. Q-carbon, rich in diamond-forming sites, enhances nucleation by interacting with diamond-forming gas species, promoting crystal growth on  $\beta$ -Ga<sub>2</sub>O<sub>3</sub>/sapphire substrates (Figure 1a). The distinct boundary highlights the effectiveness of the Q-carbon interlayer in differentiating nucleation and uniform coverage between Q-carbon and amorphous carbon zones. Because no shadow mask is used during PLA, the nucleation sites gradually shifted from the PLA zone to the non-laser-annealed region. Sequential high-resolution images depict a continuous and uniform coverage of the diamond layer, as illustrated in Figures 1b and c.

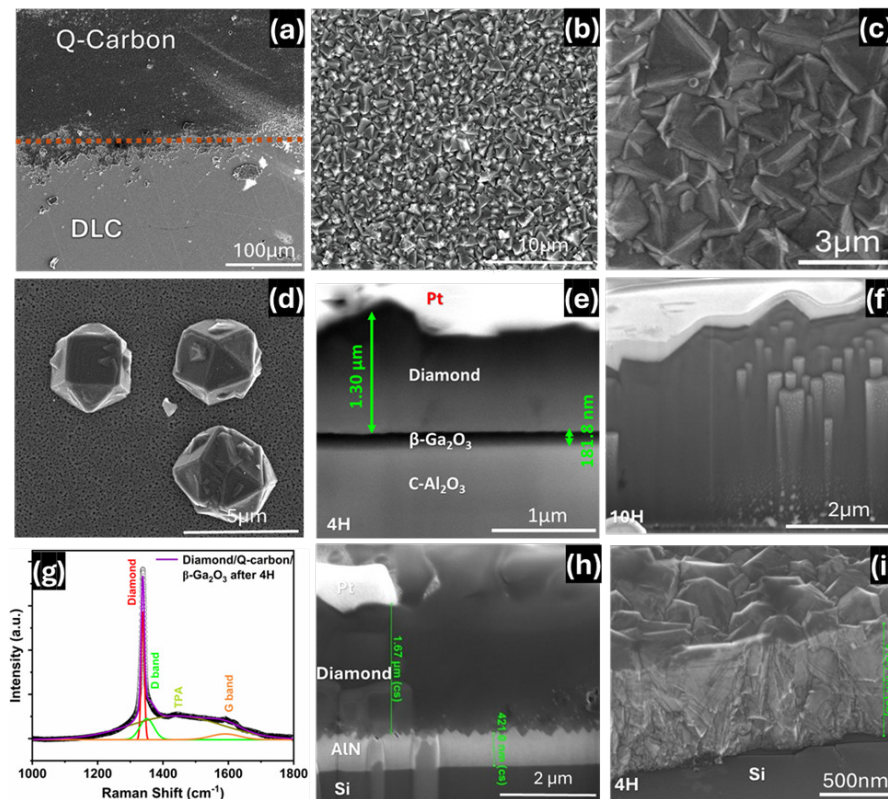


**Figure 1:** Diamond growth on  $\beta$ -Ga<sub>2</sub>O<sub>3</sub> and AlN using Q-carbon interlayer. a) SEM image of diamond film grown by HFCVD on  $\beta$ -Ga<sub>2</sub>O<sub>3</sub>/sapphire using PLA-grown Q-carbon interlayer where phase boundary differentiate between Q-carbon and DLC coated area; b) Continuous diamond film growth on Q-carbon/  $\beta$ -Ga<sub>2</sub>O<sub>3</sub>/sapphire; c) High magnification image of large area diamond formation on Q-carbon coated area; d) sporadic diamond growth on  $\beta$ -Ga<sub>2</sub>O<sub>3</sub>/sapphire; e and f) Cross-sectional SEM image of diamond grown on Q-carbon/ $\beta$ -Ga<sub>2</sub>O<sub>3</sub>/sapphire after 4H and 10H; g) Raman spectra of diamond on Q-carbon coated  $\beta$ -Ga<sub>2</sub>O<sub>3</sub> shows sharp peak at 1332.6 cm<sup>-1</sup>; h) Interfacial layer of diamond growth after 4H on Q-carbon:AlN/Si and i) Diamond growth of conventional seeded Si substrate.

In contrast, sporadic diamond growth on diamond-like carbon films (Figure 1d) emphasizes the necessity of the Q-carbon interlayer as a proper nucleation medium. The microstructure analysis unveils a five-fold twinning pattern in diamonds formed on Q-carbon, hypothesized to enhance toughness by deflecting cracks. This twinning-induced modification in crystal structure leads to increased hardness.

Investigating the nuanced aspects of diamond deposition on the Q-carbon-coated region of  $\beta$ -Ga<sub>2</sub>O<sub>3</sub>/c-Al<sub>2</sub>O<sub>3</sub> unveils significant insights into the complex interfacial layers among the substrate, Ga<sub>2</sub>O<sub>3</sub> film, and diamond, as elucidated by cross-sectional SEM images (Figure 1e & f). Following a 10K laser pulse, the  $\beta$ -Ga<sub>2</sub>O<sub>3</sub> film thickness measures approximately 180 nm. Meanwhile, the Q-carbon-coated film exhibits varying diamond thicknesses, measuring 1.30  $\mu$ m and 5.88  $\mu$ m with an increase in deposition time from 4 to 10 hours. Remarkably, generating Q-carbon on an alternative wide bandgap semiconductor material like AlN yields a similar thickness of approximately 1.67  $\mu$ m for the diamond film within the same time frame (4 hrs). Nevertheless, the limitations of cross-sectional SEM make it challenging to distinguish between the Ga<sub>2</sub>O<sub>3</sub> or AlN buffer layer and the Q-carbon interlayer. Raman spectroscopy (Figure 1g) corroborates the quality of the diamond film, with the characteristic peak at 1332.6 cm<sup>-1</sup> occurs due to the vibration of the two-interpenetrating cubic sublattices of the diamond and the peak at 1460 cm<sup>-1</sup> is connected to trans-polyacetylene (trans-PA) vibrational modes.

The absence of the 1130 cm<sup>-1</sup> peak signifies the lack of nanocrystalline trans-polyacetylene at grain boundaries. The sp<sup>2</sup>-bonded D-band peak at approximately 1360 cm<sup>-1</sup>, known as the “breathing” mode, and the in-plane stretching mode of sp<sup>2</sup>-bonded carbon in chains and rings at approximately 1580 cm<sup>-1</sup> are associated with the G band, referencing non-diamond carbon. Raman analysis reveals a high-quality, stress-free diamond film, as indicated by the peak shift from its original position (1332.0 cm<sup>-1</sup>), an FWHM of 9.28 cm<sup>-1</sup>, and a computed stress value of approximately 0.37 GPa. In contrast to the conventional nanodiamond-seeded sample depicted in Figure 1i, the nanodiamond-seeded Si substrate exhibits a lower thickness of diamond films (0.946  $\mu$ m) under identical HFCVD time and deposition parameters. As the diamond film thickness in the Q-carbon region increases, the observed growth patterns reveal a clear and well-defined faceted columnar structure (Figure 1f), particularly accentuated after 10 hours of growth. In contrast, diamond growth on a seeded Si substrate displays a random orientation with a distinctive zigzag pattern. This observation underscores the crucial role of the interface in ensuring uniform diamond growth across the thickness, thereby validating the efficacy of Q-carbon in providing abundant and high-quality nucleation sites, contributing to a higher initial deposition rate of the diamond film. This innovative approach to depositing diamonds on ultra-wide bandgap  $\beta$ -Ga<sub>2</sub>O<sub>3</sub> and AlN offers a promising avenue to tackle thermal management challenges in emerging high-power electronic devices.

## CALL FOR PAPERS

Authors are invited to submit their manuscripts for the next edition of the Texas Journal of Microscopy. The objective of the journal is to publish papers on original research and developing methods for providing prospect guidelines to research supported by all forms of microscopy. Please send your work as short communications, full articles or review articles in biological sciences, material sciences and/or education to the journal editor.

Catalina Iulia Pislariu, PhD  
[cpislariu@twu.edu](mailto:cpislariu@twu.edu)

## RESEARCH

### CHARACTERIZATION OF EJECTED PARTICLES FROM A LITHIUM-ION BATTERY DURING THERMAL RUNAWAY

CHRISTIAN A. LANDRY, PAUL O. ADEFIRANYE, SAMUEL A. MCCAULLEY, BRYCE D. HALSEY, WILLIAM F. THEILE, AND JAMES C. THOMAS

J. Mike Walker '66 Department of Mechanical Engineering, Texas A&M University, College Station, Texas

#### Abstract

The recent rise of lithium-ion battery (LIB) integration into modern society has led to an increase in hazardous scenarios for consumers via battery failure. Thermal runaway (TR) is the primary failure mode of these batteries and results in several potential hazards. The current study focused on characterization of the micro- and nano-particulates that are ejected from a LIB during TR. A state-of-the-art battery failure experiment was utilized to thermally induce TR in a Panasonic NCR 18650B LIB cell at 100% state-of-charge (SoC) in air. Subsequent microscopy and materials analysis techniques were performed on ejecta samples collected from the battery failure experiment. Scanning electron microscopy (SEM) imaging results showed a wide distribution of particle geometries and sizes ( $< 1 \mu\text{m} - \sim 2 \text{mm}$ ). Energy dispersive spectroscopy (EDS) analyses on representative SEM images provided evidence of vigorous mixing and extensive intercomponent reactions within the LIB cell during TR. X-ray diffraction (XRD) and X-ray photoelectron spectroscopy (XPS) analyses provided additional insight including the key intercomponent interactions, evidence for partial oxidation and decomposition, and the potential presence of undisclosed additives or contaminants. The approach implemented here is the first of its kind and provided valuable insight into the underlying thermodynamics and reactions that take place during LIB TR events.

**Keywords:** lithium-ion, battery safety, thermal runaway

#### Introduction

Lithium-ion battery (LIB) safety has come to the forefront of energy storage research with the advent of global 'green' energy initiatives. These batteries are rapidly being integrated into new technologies due to their efficient energy storage properties, but they are prone to catastrophic failure. LIB failure can occur by different modes (mechanical, thermal, electrical, etc.) and lead to thermal runaway (TR). (Wang et al., 2012) TR results in the combustion of the battery and leads to several different potential safety hazards. In particular, significant energy release, jet flames, toxic/flammable gas production, ejected particulates, and secondary explosions are concerns for consumer safety (Feng et al., 2018). The current study focuses on the characterization of ejected particulates from battery TR experiments because existing literature for this hazard is scarce.

Liu et. al (2018) investigated how TR affected the cathode composition of the battery via scanning electron microscopy (SEM), energy dispersive spectroscopy (EDS), and x-ray photoelectron spectroscopy (XPS). Their work highlighted how TR changes the composition of primary LIB components but did not consider the material that is ejected from the battery. Chen et. al (2020) completed the most comprehensive battery TR particulate study to date which included post-experiment SEM, EDS, and thermal decomposition experiments. However, the lack of sufficient data in their study and the available literature has limited the scope of their findings. Accordingly,

there is a need for additional studies to address existing knowledge gaps.

Typical LIBs are composed of an aluminum casing, a carbon-based anode, a metal oxide cathode, copper and aluminum current collectors, polymeric separator materials, and an electrolyte solution. Common cathode materials include lithium iron phosphate (LFP,  $\text{LiFePO}_4$ ); cobalt oxide (LCO,  $\text{LiCoO}_2$ ); nickel cobalt oxide (LNCO,  $\text{LiNi}_x\text{Co}_{1-x}\text{O}_2$ ) manganese oxide (LMO,  $\text{LiMn}_2\text{O}_4$  or  $\text{Li}_2\text{MnO}_3$ ); and nickel manganese cobalt oxide (NMC,  $\text{LiNi}_x\text{MnyCo}_{1-x-y}\text{O}_2$ ). The electrolyte solution consists of a mixture of organic solvents and a lithium salt to transport the lithium ions to/from the cathode and anode during charging/discharging. The most common salt used in LIBs is lithium hexafluorophosphate ( $\text{LiPF}_6$ ), which is mixed with solvents, such as ethylene carbonate (EC), diethyl carbonate (DEC), and dimethyl carbonate (DMC). The electrolyte materials are the most volatile in LIB systems, but separator decomposition and failure generally leads to catastrophic TR. Separator failure allows for direct cathode/anode contact, short circuiting, and exothermic reactions to take place at the cathode which release oxygen and heat. LIB surface temperatures can reach in excess of  $500 \text{ }^\circ\text{C}$ . This high-temperature environment yields combustion reactions that produce metal oxides, carbon soot, and a wide variety of other reaction product species.

The goal of the current study was to investigate the material that is ejected from a LIB during TR using modern microscopy and materials analysis techniques. These analyses potentially provide a better thermodynamic understanding of the reactions taking place within a LIB undergoing TR and allow for identification of hazardous ejected materials. In order to achieve this goal, a sample of ejected material was procured from a LIB TR experiment and subsequently evaluated with SEM/EDS, XPS, and x-ray diffraction (XRD) techniques. The following two sections detail the experimental set-up and observations and findings, respectively. Key findings and areas for future research are provided in the Conclusion section.

### Experimental Methods

A constant-volume bomb has been developed at Texas A&M University to run LIB TR experiments, as shown in Fig. 1. The experimental design allows for direct control of ambient gas composition and pressure. TR is initiated by a programmable proportional-integral-derivative (PID) controller connected to a flexible film heater. The heater is affixed to the surface of a single LIB cell that is mounted within the vessel. Multiple thermocouples allow for the monitoring and recording of cell surface temperature and the volume headspace. Transient pressure and cell voltage diagnostics are also included. The addition of a steel housing within the vessel allows for the containment of the ejected particulates for post-test collection. The presence of large windows will allow for future integration of optical-based diagnostics. The present study considered the ejected material collected from a Panasonic NCR 18650B LIB cell undergoing TR. The Panasonic cell was a LNCO-based battery with a graphite (C) anode, standard aluminum (Al) and copper (Cu) current collectors, a 2:1 polyethylene (PE):polypropylene (PP) separator, and an electrolyte mixture consisting of LiPF<sub>6</sub> in a 1:1:1 mixture of EC:DEC:DMC (Panasonic NCR18650B, 2016; NCR-18650B, 2020).

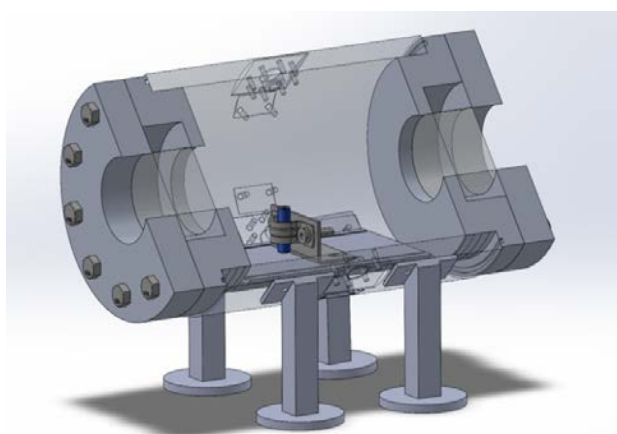


**Figure 1.** State-of-the-art battery failure experiment recently developed at Texas A&M University.

The cell was fully charged to 100% state-of-charge (SoC) prior to the experiment and the vessel was filled with dry air at ambient pressure. The cell was heated at a rate of approximately 10 K/min until TR was thermally initiated. The ejected material was collected post-experiment after the system cooled.

The Microscopy and Imaging Center (MIC) at Texas A&M University (TAMU) houses the TESCAN VEGA SEM and Aztec software used to image and characterize the elemental composition of the ejected material. SEM samples were prepared by dispersing ejected debris powder on double-sided carbon tape atop an aluminum pedestal. The images were taken using a Tungsten thermionic emission system at 30 kV within a high vacuum under varying magnifications. XRD analysis was carried out by the TAMU X-Ray Diffraction Laboratory (XRDL) and used PDF-4+ software from the International Centre for Diffraction Data (ICDD) to identify compounds. XPS analysis was performed by the TAMU Materials Characterization Facility (MCF). The electronic states of elements and compounds were identified with the CasaXPS software and National Institute of Standards and Technology (NIST) XPS Database. The samples for the XRD and XPS analyses were prepared in accordance with their respective facility's guidelines.

### Results and Discussion

Representative SEM images of collected particles and EDS mapping are provided in Figs. 2-4. Numerous images were collected during the study and only a few representative images are provided here due to space limitations.

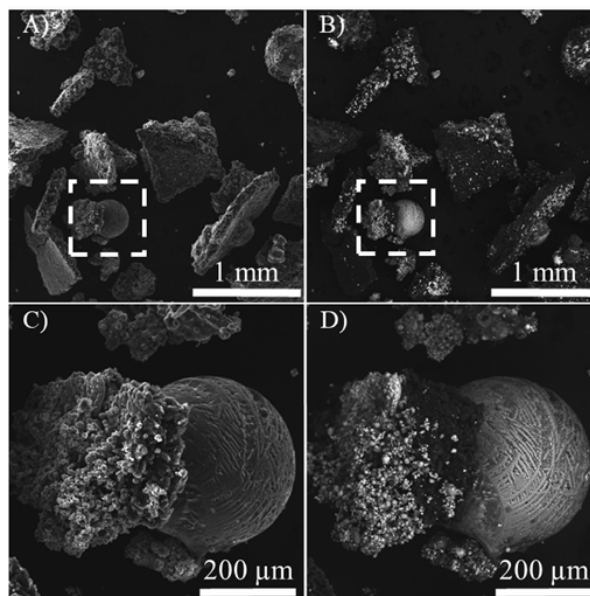


**Figure 2.** Representative sample of SEM images taken of a collection of macro- and micro-particles. A) 100x magnification image with a secondary electron (SE) detector. B) 100x magnification image with a backscatter electron (BSE) detector in which heavier elements are illuminated more. C) 450x magnification image of a single agglomerate particle with a SE detector. D) 450x magnification image of a single agglomerate particle with a BSE detector.

A wide distribution of particle sizes ( $< 1 \mu\text{m}$  –  $\sim 2 \text{mm}$ ) and geometries that were ejected from the battery during TR were observed in the SEM images. Various nano-particles were observed in isolation and on the surface of larger particulates. Particle size distributions of LIB TR ejecta is an important parameter because these particulates are locally dispersed in the atmosphere during TR events and pose an inhalation potential hazard to humans in the vicinity. A quantitative particle size distribution would be beneficial but requires additional techniques, such as laser-based size analysis and TEM imaging of nano-particles.

The atomic and molecular composition of the ejected particles can potentially elucidate information about reactions taking place during TR and the underlying physical phenomena and thermodynamics. EDS mapping (Fig. 3) was coupled with the SEM images to distinguish the atomic surface composition of particles. The particle shown in the higher-magnified portion of Fig. 3 contains isolated agglomerates from the positive (Al) and negative (Cu) current collectors, cathode (Co, Ni, and O), and anode (C). Elements corresponding to each of these components were not primarily localized to specific regions of the particle and intercomponent mixing and reactions are clearly present. For example, the right portion of this particle clearly contains highly correlated Al and Cu from the positive and negative current collector materials, respectively, which the furthest apart inside the cell's 'jelly roll'. This observation indicates vigorous mixing of cell components during the TR process.

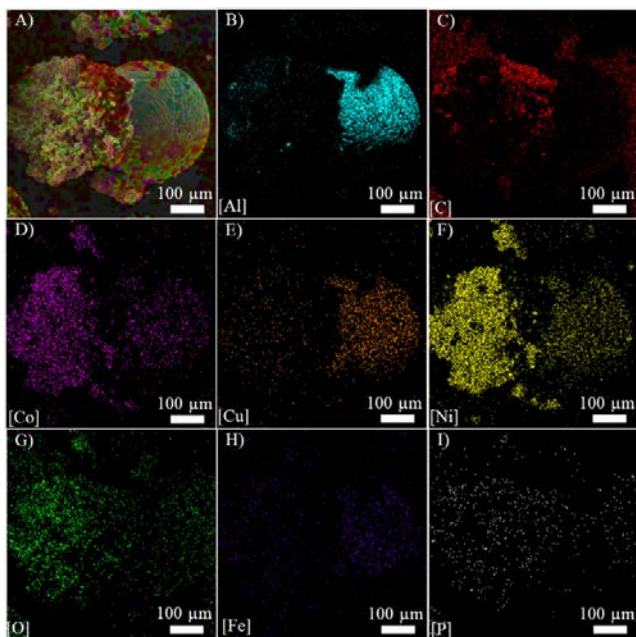


**Figure 3.** EDS elemental mapping of a single agglomerate particle. A) Full elemental mapping of the particles of the elements detected which were B) Aluminum (Al), C) Carbon (C), D) Cobalt (Co), E) Copper (Cu), F) Nickel (Ni), G) Oxygen (O), H) Iron (Fe), and I) Phosphorous (P).

The corresponding area in Fig. 3 associated with these materials is also correlated with the presence of Fe, Ni, Co, P, and O. Fe is a common additive found in the positive current collector; Ni and Co originate from the cathode material; and P is derived from the lithium salt in the electrolyte. The strong correlation between all these elements in a single agglomerate particle further suggests vigorous mixing of all components within the cell during the TR process. This particular agglomerate appears to be a partially oxidizer intermetallic reaction product. The widespread presence of O suggest most of the components are partially or fully oxidize during TR and the similar widespread presence of P indicates the electrolyte reacts with all cell components, as well.

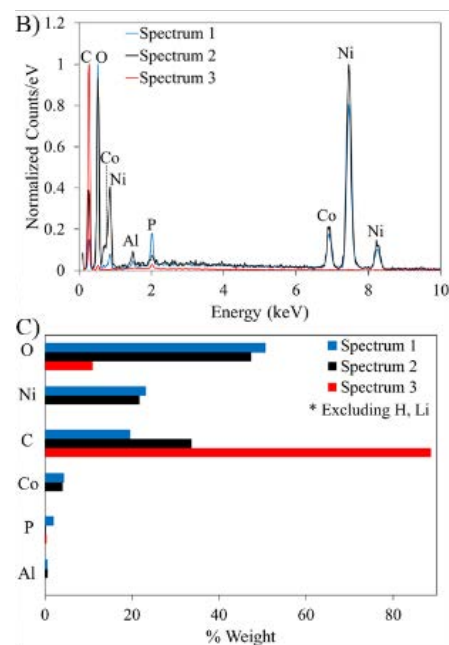
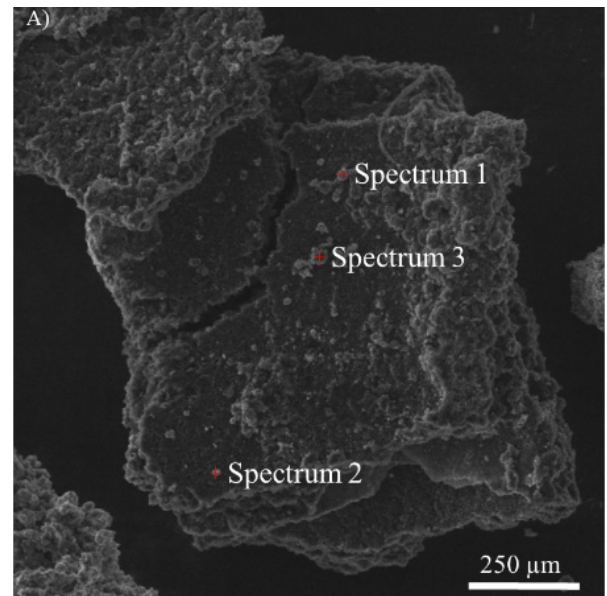


**Figure 4.** SEM and EDS point spectrum analysis for smaller particles on the surface of a larger particle. A) 250x magnification image using a secondary electron detector with respective elemental B) counts and C) weight percentage for each spectrum.

An additional representative microparticle is shown in Fig. 4 with accompanying EDS scan data provided as insets. The particle is mostly composed of C which suggests it originates from the anode. The particle surface is covered in much smaller particles with varying compositions, as shown with the EDS data. The wide variation in the EDS data illustrates the variety of products that are formed during the TR process. The EDS inset in Fig. 3 also notes that lighter elements (e.g., H and Li) are excluded from the EDS analysis because they are not detectable by this method. An alternative elemental identification method, such as wavelength dispersive spectrometry (WDS), may provide additional insight because of its superior resolution and capability to identify elements with lower EDS energies (< 1 keV), except hydrogen and helium.

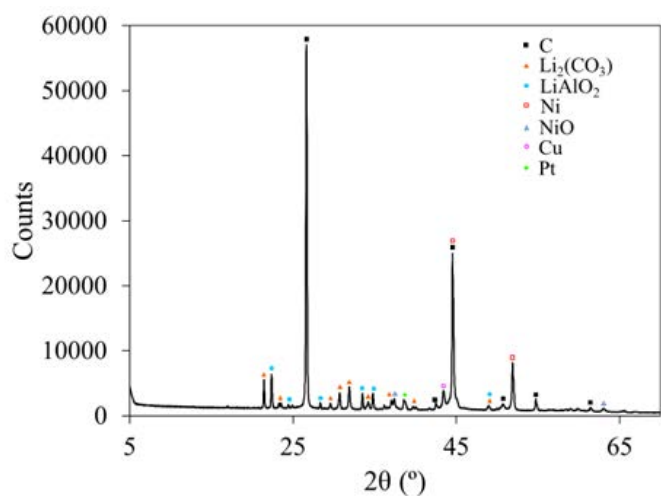


**Figure 5.** XRD data for a powder sample with peaks identified by diffraction angle.

The XRD analysis provided in Fig. 5 allowed for the identification of crystalline structures present in the collected sample. The presence of C, lithium carbonate ( $\text{Li}_2\text{CO}_3$ ), lithium aluminate ( $\text{LiAlO}_2$ ), Ni, NiO, Cu, and Pt were all observed in the XRD data. Lithium carbonate is commonly formed as part of the solid electrolyte interphase in LIBs, so it may have been present before TR or formed during TR reactions between the electrolyte and cathode. Lithium aluminate is an oxidized intermetallic compound which is not commonly found in standard LIBs and likely formed during TR due to reactions between the electrolyte, positive current collector, and cathode. Partial oxidation, or decomposition, was observed for the cathode Ni material as evidenced by the presence of metallic (Ni) and oxidized (NiO) compounds. The presence of Pt in the XRD data was unanticipated. Platinum is highly conductive and being considered for high-performance battery systems but is not standard in most LIB cells. However, the exact composition of the cell evaluated here is not disclosed in the open literature due to proprietary reasons. The observed Pt may be an additive in the battery or a contaminant from the

experimental procedures (i.e., from the flexible film heaters).

Low-resolution XPS data are provided in Fig. 6a which identified more elements (Na, K, Sn, Ca, Cl, and Si) that were not disclosed by the manufacturer as being present in the cell's composition. Once again, these elements may be derived from additives or a contaminant from the experimental procedures. Regardless, these observations suggest a highly controlled experiment and post-test collection strategy may be required to avoid sample contamination.

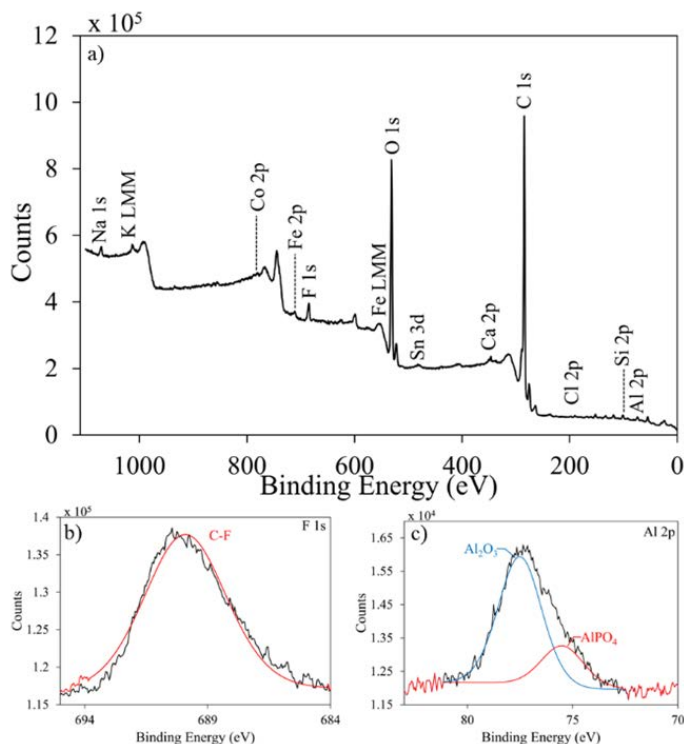


**Figure 6.** XPS data for debris ejected during LIB TR. A) Low-resolution full spectrum scan; and high-resolutions scans of the B) F1s and C) Al2p peaks.

Representative high-resolution scans of the F1s and Al2p peaks are shown in Figs. 6b and 6c, respectively. Additional high-resolution XPS data were collected but are not provided here for brevity. Curve fitting in CasaXPS was used to identify different compounds that were likely present at the elements' respective electronic state. A carbon-fluorine (C-F) compound was the only appreciable compound identified for the F1s peak. This compound could be present as an undisclosed fluoropolymer additive, such as polyvinylidene fluoride (PVDF), but is more likely present due to reactions between the electrolyte's lithium salt and anode. Aluminum oxide ( $\text{Al}_2\text{O}_3$ ) and aluminum phosphate ( $\text{AlPO}_4$ ) were identified as compounds that comprised the Al2p peak. The observation of  $\text{Al}_2\text{O}_3$  in the XPS data and not the XRD data indicates it is amorphous rather than crystalline. The presence of  $\text{AlPO}_4$  provided further evidence of reactions between the positive current collector and electrolyte.

## Conclusion

The current study evaluated particles ejected from a LIB during TR with microscopy and materials analysis techniques. The experimental and subsequent analysis protocol are the first of its kind and provided valuable insight into the underlying thermodynamics and reactions that take place during LIB TR events. Particle sizes were observed in a wide range of micro- and nano-sizes with varying geometries. SEM images with EDS analyses enabled investigation of the atomic composition on representative particles. Individual battery components were distinguishable in the analyses, but vigorous mixing during TR and reactions between all components were evident. XRD and XPS analyses provided further evidence of intercomponent reactions and elucidated key interactions for condensed phase product species. Partial oxidation or decomposition of the cathode materials was also observed in the XRD data. The lack of a detailed battery composition from the manufacturer hindered the authors' capability to fully discern whether some elements/compounds were additives or experimental contaminants. The findings from this study and future follow-on studies will enable a better understanding of phenomena and reactions that take place between battery components during TR and quantification of their hazards.

## Funding

This work was partially funded by the Texas Society of Microscopy (TSM) Undergraduate Small Grant Program and the Sigma Xi Grants in Aid of Research (GIAR) program. Additional funding came from the National Science Foundation (NSF) Graduate Research Fellowship Program (GRFP) under Grant No. 2139772.

## References

- Wang, Q., Ping, P., Zhao, X., Chu, G., Sun, J., and Chen, C. (2012) Thermal Runaway Caused Fire and Explosion of Lithium-Ion Battery. *Journal of Power Sources*. 208:210-224.
- Feng, X., Ouyang, M., Liu, X., Lu, L., Xia, Y., and He, X. (2018) Thermal Runaway Mechanism of Lithium-Ion Battery for Electric Vehicles: A Review. *Energy Storage Materials*. 10(1):246-267.
- Liu, X., Ren, D., Hsu, H., Feng, X., Xu, G. L., Zhuang, M., Gao, H., Lu, L., Han, X., Chu, Z., Li, J., He, X., Amine, K., and Ouyang, M. (2018) Thermal Runaway of Lithium-Ion Batteries without Internal Short Circuit. *Joule*. 2(10):2047-2064.
- Chen, S., Wang, Z., and Yan, W. (2020) Identification and Characteristic Analysis of Powder Ejected from a Lithium Ion Battery during Thermal Runaway at Elevated Temperatures. *Journal of Hazardous Materials*. 400(1):1-20.
- Safety Data Sheet – Panasonic NCR18650B (2016) Shenzhen SEM Test Technology Company, Ltd.
- Lithium-Ion – NNP + HRL Technology, NCR-18650B (2020) Panasonic Energy Company, Ltd.

## CHARACTERIZATION OF ISOTROPIC AND ANISOTROPIC PARTICLES DISPERSED IN LUBRICATING AUTOMOTIVE GREASES USING SCANNING ELECTRON MICROSCOPY (SEM) COUPLED WITH ENERGY DISPERSIVE X-RAY SPECTROSCOPY (EDS)

JARED ESTEVANES AND GERALDINE MONJARDEZ

Department of Forensic Science, College of Criminal Justice, Sam Houston State University, Huntsville, TX, U.S.  
Corresponding author: Jared Estevanes - jae031@shsu.edu

## Abstract

In the context of a forensic case, lubricating automotive greases may be submitted to a laboratory for identification as general unknowns, may be recovered on the garments of a suspect allegedly involved in events under investigation, or they may be found as dropped stains on the ground or on objects at a crime scene. Microscopic examinations previously conducted on grease samples showed the presence of various particle types dispersed in pure, unused automotive greases, which were classified into three categories: opaque, isotropic and anisotropic. These particles differed considerably between different grease samples. It was uncovered that the opaque particles were solid lubricant additives within the greases and displayed potentially discriminating properties.

We report the characterization of the isotropic and anisotropic particles by Scanning Electron Microscopy-Energy Dispersive X-ray Spectroscopy (SEM-EDS). The characterization of the isotropic and anisotropic particles proved more challenging in comparison to the opaque particles due to smaller size in conjunction with sample interference and charging. To address these issues, we used a combination of SEM parameter development and the variable pressure mode at 60 Pa.

The elemental composition of the isotropic and anisotropic particles included lighter elements such as sulfur and calcium. The analysis of the isotropic particles remained difficult due to their smaller size and the compromises that had to be made in the instrumental setup, which prevented imaging at higher magnifications. The elemental data and light microscopy indicated that the anisotropic particles were solid lubricants of a different type compared to the opaque particles, specifically calcite (CaCO<sub>3</sub>).

**Keywords:** Forensic science; trace evidence; automotive lubricating grease; microscopy; SEM-EDS

## 1. Introduction

Currently, in practice, the forensic subdiscipline of trace materials analysis is underexploited, with the collection and analysis being too often focused on a restricted number of trace materials, such as paint, hair, fibers, and glass (Desiderio et al., 2021). While other trace materials such as ignitable liquid residue (Stauffer et al., 2008) and gunshot residue (Smyth Wallace, 2021), are routinely analyzed, there are many non-routine materials that could contribute to the clarification of cases being investigated, including the possible association of a motor vehicle with a crime victim following a hit-and-run. According to the National Highway Traffic Safety Administration (NHTSA), 91% of pedestrians killed in vehicular crashes involved a single vehicle. For these crashes, 1 in 5 were struck in hit-and-run crashes (NHTSA Traffic Safety Facts, 2017).

The present research focuses on the forensic examination of pristine grease samples, specifically the characterization of isotropic and anisotropic particles dispersed in lubricating automotive greases using SEM-EDS. The presence of microscopic particles in many automotive greases that were not present in brake fluids or transmission fluids was first reported by Lewis et al [5]. Brightfield and polarized light microscopy revealed that these particles can be classified into three categories: opaque, isotropic and anisotropic, and differed considerably between different grease samples. It was found that the opaque particles were solid lubricant additives within the greases.

SEM-EDS is well established in forensic laboratories and enables analyzes of various trace materials such as paint (Henson et al., 2001; Weimer et al., 2021), glass (Koons et al., 2018), and gunshot residue (GSR) (Nesbitt et al., 1976; Wolten et al., 1979; Rudzitis et al., 1980). Previous attempts to analyze isotropic and anisotropic particles proved challenging compared to the opaque particles. By gaining a deeper understanding of how the morphology and/or elemental composition of these particles relate to their challenging analysis, we developed an SEM-EDS method to characterize them.

## Materials and Methods

*Samples.* Fourteen automotive greases containing the particles of interest were selected from a dataset of thirty-five greases collected from automotive and hardware US national chain retailers. The samples shown in Table 1 were a mix of different end uses, including multi-purpose, heavy duty, and marine.

**Table 1. Brands and Types of Grease Samples**

Sample #	Brand	Grease Type
002	Lucas	Marine
003	Lucas	Red "N" Tacky #2
008	Masterpro	Super White
009	Masterpro	Wheel Bearing
010	Mobil1	Synthetic
012	Mystik	JT-6 Multi-Purpose
013	Nano Pro MT	Hi-Temp
016	Sta-Lube	Extreme Pressure Sta-Plex
017	Sta-Lube	Lithium General Purpose
021	SuperTech	Marine
024	Valvoline	Cerulean
032	WD-40	Marine
033	WD-40	Specialist Heavy-Duty High Temperature
035	WD-40	Specialist Superior Performance True Multi-Purpose

*Extraction of particles.* The extraction scheme was developed based on the procedure outlined by Snyder et. al, 2016. Half of a gram of each sample was placed into a 20 mL glass vial (Thermo Fisher Scientific, Waltham, MA) with 15 mL of D-limonene purchased from VWR (Randor, PA). The vial was capped, and the sample was left to dissolve for 15 minutes with occasional swirling. After dissolving, the solution was gravity filtrated for 1 hour, using a 125 mm diameter Whatman No. 1 filter paper (Cytiva, Marlborough, MA). The filter paper was then removed and allowed to air dry for an additional hour in the fume hood.

*SEM-EDS analyses.* After extraction, the flakes recovered from the filter paper were selected for SEM-EDS analysis. Particles within the greases were located using a Hitachi™ backscatter detector (Hitachi, Ciyoda City, Japan) and were visualized using their contrast to the background. After extraction, the dried residues were flattened between two glass slides prior to be stamped on a 12.74 mm circular stub pin mount for gunshot residue analysis (Electron Microscopy Sciences, Hatfield, PA). The analysis was conducted with a SEM SU3500 scanning electron microscope (Hitachi, Chiyoda, Tokyo, Japan) using the backscatter detector and variable pressure mode at 60 Pa. EDS data was obtained with a Quantax XFlash® 6 energy dispersive spectrometer from Bruker Corp. (Billerica, MA) with the EDS calibrated to a copper tape standard by 3M (Saint Paul, MN). An accelerating voltage of 25 kV with a working distance of 10 mm was used. The elemental composition of the particles was determined using Quantax Espirit software (Bruker, Billerica, MA). Seven measurement replicates were taken for each sample.

## Results

*SEM-EDS analysis of anisotropic particles.* Anisotropic particles were identified using brightfield and Polarized

Light Microscopy (PLM) in fourteen greases in which this particle type was abundant (Figure 1 A and B). The sizes of the anisotropic particles ranged from <10  $\mu\text{m}$  to over 40  $\mu\text{m}$ . Figure 1C shows the image obtained with the backscatter detector, which allowed the careful selection of measurement points for each sample.

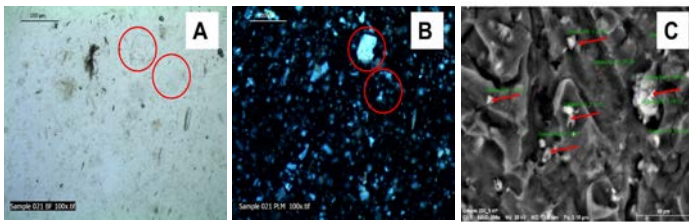


**Figure 1.** Photomicrographs of sample 021 SuperTech Marine. A) bright field illumination and B) double polarization, showing the anisotropic particles circled in red. Panel C) image was acquired with the SEM backscatter detector showing the particles selected for EDS analysis with red arrows. Each measurement location is indicated with green text, provided by the software, and the red arrow for added visibility.

Table 2 shows the normalized elemental abundance mean values in % for all fourteen greases analyzed.

Sample	Average normalized mass concentration [%]											
	Na	Al	Si	P	S	K	Ca	Zn	Mo	Sb	Fe	I
2	0.60	0.11*					0.27*					
4							26.32					
8		0.24*					6.39	8.82				
9					.40*	1.15	1.71	0.18*				
10				0.20	0.28*			0.26*				
12			1.30		0.21*	3.76	10.80				1.06	
13	0.15*			1.34	0.12*		4.92			0.26*		
16				0.52	2.55		12.73	4.79	1.68			29.38
17			0.28*		0.67		3.13		2.24			
21					0.70		6.64			2.09		
24					1.34		7.86					
32					0.15*		20.00					
33					0.32*		13.34	0.28*				
35					0.50		23.62					

(\*) indicates normal mass concentration less than 0.5%

**Table 2.** Normalized mass concentrations (%) of the elements identified in anisotropic particles through SEM-EDS analysis.

Calcium in levels above 1% /wt. was detected in all greases, except for samples 002 and 010. Iodine was detected with relatively high abundance (29.38%) in sample 016 Sta-Lube Extreme Pressure Sta-Plex only. Detection of zinc in levels above 1% /wt. was observed in samples 008 (8.82%) and 016 (4.79%). Sulfur in levels above 1% /wt. was also detected in samples 016 (2.55%) and 024 (1.34%). An SEM image collected with the backscatter detector and the associated EDS map obtained for calcium highlighted the localization of calcium in the particles for grease 033 (Figure 3). This trend was seen across all greases that contained calcium.

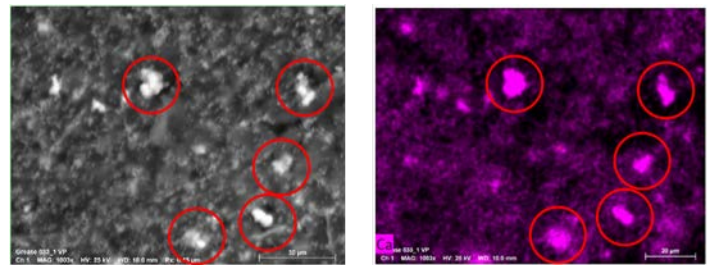


**Figure 2.** Image obtained with the SEM backscatter detector showing the particles selected for EDS analysis circled in red (left) and for the associated EDS map for calcium

## Discussion

The present study focused on the characterization of microscopic particles in new unused greases. While elements identified in the greases can also be found in other automotive fluids such as motor oil and transmission fluids, the presence of solid lubricant additives can be considered as discriminating detectable properties of greases in an automotive context (Casserly et al., 2018; Day, 2018). When selecting targets for the EDS analysis of the isotropic and anisotropic particles, the SEM backscatter detector allowed for their detection as they produced visible contrast to the carbon thickener background. Other techniques such as ICP-OES permits the quantitative elemental composition of the sample to be determined; however, using SEM to detect the particles proved to be a significant advantage as it allowed the careful selection of measurement points and therefore increased the confidence in attributing EDS data to the particles. Particles were identified by SEM based on their morphology, size, and contrast, and were assessed by comparison with photomicrographs obtained using brightfield illumination. Previous attempts to analyze the particles were impeded by sample charging which caused interference with imaging and the EDS detector. Charging and interference were ultimately due to the presence of solvent and oil residue left in the sample after extraction. Using the variable pressure mode allowed limited pressure into the chamber, which mitigated the volatilization of solvents into the space within the sample chamber, and thus limited the interference.

On the down side, this instrumental setup prevented the use of the secondary electron detector and limited the magnification achievable within the SEM. For this reason, it was not possible to acquire clear images at magnifications higher than 2000x. This limitation prevented the imaging and measurement of the individual isotropic particles, as their size was less than 5  $\mu\text{m}$  in diameter. The EDS mapping data revealed that no element heavier than Zn was localized to any particular area within the grease. It can therefore be surmised, that the isotropic particles contain elemental compositions that are equal to, or lighter than Zn, even if the individual particles themselves could not be visualized or analyzed. The use of a carbon sputter coater may yield better

visualization in this aspect and allow for elemental characterization.

The study also showed that every grease tested contained calcium in levels above 1% /wt. except for samples 002 and 010. Industrial applications can include the use of calcium sulfonate thickeners as an alternative to lithium-based thickeners for the grease. Calcium sulfonate greases have advantages over traditional lithium-based greases in that they have better corrosion protection, assist in lower wear on the components, and have higher extreme pressure performance. The manufacturing process of calcium sulfonate greases is beyond the scope of this work; however, the creation of the mineral calcite ( $\text{CaCO}_3$ ) is a desired byproduct of the thickening process (Sniderman and Mackwood, 2016). The calcite produced within the grease acts as a solid lubricant, especially at temperatures above 600 °F (Ward, 2006; Mackwood and Brown, 2001; John et al., 1998). Additionally, the optical properties of the anisotropic particles are consistent with calcite minerals. Unfortunately, the only grease within the sample set that is stated as using calcium sulfonate thickener was grease 035. However, the microscopy and EDS results suggests the remaining 13 greases still use calcium sulfonate as a grease thickener in conjunction with a lithium-based thickener, or add calcite separately as a solid lubricant.

The other elements identified were sulfur and zinc that are known to be “performance additives” within greases and their signal can originate from various components within the grease, such as additives or thickeners (Rawat and Harsha, 2019). Therefore, it is difficult to determine the source of these elements as it pertains to individual grease formulations.

## Conclusion

This study showed that the abundance of elements detected within the sample set via SEM-EDS suggests that the anisotropic particles were most likely solid lubricant additives, more specifically calcite ( $\text{CaCO}_3$ ). SEM allowed to visually select the extracted anisotropic particles by shape, size, and general morphology.

The identity of the isotropic particles, as it relates to the grease formulation, is still under investigation, however it was discovered that these particles contains elements that are equal to or lighter than Zn. Further work will be necessary for the analysis of these particles due to their size (<5  $\mu\text{m}$ ) and interferences from the matrix. The analysis of the pristine greases with another technique such as inductively coupled with plasma/optical emission spectroscopy (ICP-OES) could be beneficial. While the limitation of ICP-OES for this particular application is its inability to target the individual particles, it enables a quantitative analysis of the elemental composition of a grease sample as a whole. Additionally, the change in microscopic and elemental composition of the greases after use within a vehicle must be studied.

The use of SEM-EDS for the characterization of grease samples proved to be beneficial in the analysis and identification of particle types within the greases, with potential for discrimination. Currently, greases are not commonly submitted as forensic evidence, however the greases’ microscopic and elemental features show potential evidentiary value, and thus expansion of trace materials to include this type of compound must be considered. Using these non-routine materials could prove useful in the investigation of criminal cases, including linking a suspect vehicle to a crime scene, or victim.

## Funding

This work was funded by the 2022 Small Grant Program awarded by the Texas Society for Microscopy (TSM) and the 2021 Research Grant Award awarded by the American Society of Trace Evidence Examiners (ASTEE).

## References

- Desiderio, V.J., Taylor, C.E., Daéid, N.N. eds., Handbook of trace evidence analysis, First edition, John Wiley & Sons, Inc., Hoboken, NJ, 2021.
- Stauffer, E., Dolan, J.A., Newman, R. Fire debris analysis, Academic Press, Boston, Mass, 2008.
- Smyth Wallace, J. Chemical Analysis of Firearms, Ammunition, and Gunshot Residue, CRC Press, S.I., 2021.
- NHTSA, Traffic Safety Facts 2017 Data, 2019. <https://crashstats.nhtsa.dot.gov/Api/Public/ViewPublication/812681>
- Lewis, A., Day, J., Buzzini, P. Conceptualization of assessing the evidential value of vehicular transmission fluids, brake fluids, and lubricating greases, *Proceedings of Inter/Micro 2019 conference*. McCrone Research Institute, Chicago, IL
- Henson, M.L., Jergovich, T.A. Scanning electron microscopy and energy dispersive X-ray spectrometry (SEM/EDS) for the forensic examination of paints and coatings, Taylor & Francis: London, 2001.
- Weimer, R., Wright, D., Hodgins, T. Paints and polymers, in: V.J. Desiderio, C.E. Taylor, N.N. Daéid (Eds.), Handbook of Trace Evidence Analysis, First edition, John Wiley & Sons, Inc., Hoboken, NJ, 2021.
- Koons, R., Buscaglia, J., Bottrell, M., Miller, E. Forensic glass comparisons, in: R. Saferstein, A.B. Hall (Eds.), Forensic Science Handbook, Third edition, CRC Press, Boca Raton, FL, 2018.
- Nesbitt, R.S., Wessel, J.E., Jones, P.F. Detection of gunshot residue by use of the scanning electron microscope, *J Forensic Sci.* 21, 1976, 595–610.
- Wolten, G.M., Nesbitt, R.S., Calloway, A.R., Loper, G.L., Jones, P.F. Particle Analysis for the Detection of Gunshot Residue. I: Scanning Electron Microscopy/Energy Dispersive X-Ray Characterization of Hand Deposits from Firing, *J. Forensic Sci.* 24, 1979, 10848J.
- Rudzitis, E. Analysis of the Results of Gunshot Residue Detection in Case Work, *J. Forensic Sci.* 25, 1980, 11300J.
- Snyder, C.A., Mayotte, D., Donahue, C.J. Analysis of the Thickening Agents in Automotive Greases by GC-MS, *J. Chem. Educ.* 2006, 83, 902.
- Casserly, E., Springer, S.P. The Effect of Base Oils on Thickening and Physical Properties of Lubricating Greases, 2018, 6.

Day, J. The Characterization and Discrimination of Transmission Fluids, Brake Fluids, and Vehicular Greases, 2018.

Sniderman, D., Mackwood, W. Calcium sulfonate complex greases. *Tribology and Lubrication Technology*, 2016

Ward, B. Understanding Calcium Sulfonate Thickeners. The Lubrizol Corporation. 2006. <https://www.machinerylubrication.com/Read/909/calcium-sulfonate-thickeners>

Mackwood, W., Brown, K.J. Proper Grease Selection Reduces Steam Valve Maintenance. NLGI 2001, 66(4).

John, P.J., Prasad, S.V., Voevodin, A.A., Zabinski, J.S. Calcium sulfate as a high temperature solid lubricant. *Wear* 1998;219(2):155–61.

Rawat, S., Harsha, A.P. Chapter 9: Current and Future Trends in Grease Lubrication, in: *Automotive Tribology*, Springer, 2019: pp. 147–182.

## TECHNICAL ABSTRACTS Spring 2024

**TERS IMAGING: A UNIQUE TECHNIQUE FOR NANOSCALE CHARACTERIZATION OF STRUCTURAL PECULIARITIES IN 2D SEMICONDUCTORS AND THEIR LATERAL AND VERTICAL HETEROSTRUCTURES.** ANDREY KRAYEV HORIBA Scientific, Piscataway, NJ 08854

After a brief introduction of the tip enhanced spectroscopy (TERS) technique and instrumentation, recent advances in TERS and TEPL (tip enhanced photoluminescence) characterization of 2D semiconductors, in particular their lateral and vertical heterostructures will be discussed.

We will demonstrate how the novel, contamination-free technique of dry transfer of 2D semiconductor crystals grown on Si/SiO<sub>2</sub> or sapphire to metallic (gold and silver) substrates opens new possibilities in nanoscale Raman and PL characterization of the lateral, vertical and complex vertical/lateral heterostructures.

As an example we will discuss TERS characterization of the non-uniformity of the junction line in MoS<sub>2</sub>/WS<sub>2</sub> lateral heterostructures (Garg et al., 2022), nanoscale layer decoupling in twisted hetero-bilayers of WS<sub>2</sub> and WSe<sub>2</sub> (Rodriguez et al., 2022) and the importance of comprehensive nanoscale Raman characterization with several excitation wavelengths, both resonant and below-the-bandgap non-resonant for understanding of the composition of the complex vertical/lateral WS<sub>2</sub>/WSe<sub>2</sub> heterostructures and the nature of observed Raman modes (Krayev et al., 2022).

In the course of the discussion, we will demonstrate the cross-correlation of the TERS data with other observables provided by scanning probe microscopy such as topography, surface potential and photocurrent which makes the interpretation of the TERS data more

straightforward and enables direct link between the spectroscopic data provided by TERS and industrially important characteristics of the 2D semiconductors and their junctions with the metallic electrodes (Velický et al., 2020).

### References

Garg, S., Fix, J. P., Krayev, A.v, Flanery, C., Colgrove, M., Sulkanen, A. R., Wang, M., Liu, G.-Y., Borys, N. J., Kung, P. Nanoscale Raman Characterization of a 2D Semiconductor Lateral Heterostructure Interface. *ACS Nano* 2022, 16 (1), 340–350. <https://doi.org/10.1021/acsnano.1c06595>

Rodriguez, A., Krayev, A., Velický, M., Frank, O., El-Khoury, P.Z. Nano-optical Visualization of Interlayer Interactions in WSe<sub>2</sub>/WS<sub>2</sub> Heterostructures *J. Phys. Chem. Lett.* 2022, 13, 25, 5854–5859; <https://doi.org/10.1021/acs.jpcclett.2c01250>

Krayev, A., Chen, P., Terrones, H., Duan, X., Zhang, Z., Duan, X. Importance of Multiple Excitation Wavelengths for TERS Characterization of TMDCs and Their Vertical Heterostructures. *The Journal of Physical Chemistry C* 2022, 126 (11), 5218–5223. <https://doi.org/10.1021/acs.jpcc.1c10469>

Velický, M., Rodriguez, A., Bouša, M., Krayev, A.v., Vondráček, M., Honolka, J., Ahmadi, M., Donnelly, G. E., Huang, F., Abruña, H. D., Novoselov, K. S., Frank, O. Strain and Charge Doping Fingerprints of the Strong Interaction between Monolayer MoS<sub>2</sub> and Gold. *The Journal of Physical Chemistry Letters* 2020, 11 (15). <https://doi.org/10.1021/acs.jpcclett.0c01287>

**INVESTIGATING 2D-MATERIALS USING CORRELATIVE SPECTROSCOPY AND MICROSCOPY.** TIM S NUNNEY, PAUL MACK, ROBIN E SIMPSON, HSIANG-HAN TSENG  
Thermo Fisher Scientific, East Grinstead, West Sussex, UK.

Across a wide range of application areas, understanding the chemistry and structure of surfaces and interfaces is crucial. In the last fifty years, X-ray photoelectron spectroscopy (XPS) has become established as a one of the key techniques for measuring surface and interface chemistry, and advances in instrumentation have enabled it to keep pace with the requirements for both academia and industry. XPS can deliver quantified surface chemistry measurements, and by using depth profiling, an understanding of layer and interfacial chemistry, but the limit on spatial resolution for XPS can prevent it from determining how the surface structure is related to the measured chemical properties. For example, how the changing morphology of the surface during a depth profile could influence the measured composition would be challenging to determine using just XPS.

Other experimental techniques which are unable to match the surface selectivity of XPS can provide complementary information to extend the data from XPS. Electron microscopy can provide high resolution imaging, with elemental composition provided by

energy dispersive X-ray microanalysis, but without the same surface selectivity seen with XPS or Auger electron spectroscopy (AES). This can be a perfect complement to XPS analysis, so long as the same points of interest can be identified. Molecular spectroscopy, such as FTIR or Raman, can also provide complementary information to XPS, albeit with different sampling depths, which can be extremely useful to validate measurements or confirm particular molecular structures using the wide range of spectral libraries available for those techniques.

In this presentation, we will describe how a correlative approach using both surface analysis instrumentation and scanning electron microscopy can be used to characterize 2D nanomaterials. Samples of MoS<sub>2</sub> grown on Si substrates have been investigated using XPS, Raman and SEM to determine their composition and structure. To facilitate co-alignment of the analysis positions when moving between the instruments, special sample carriers and software alignment routines have been developed.

## MACHINE-VISION ASSISTED IN SITU TRANSMISSION ELECTRON MICROSCOPY.

GABRIELA MENDOZA, DYLAN WOOD, MADELINE DRESSEL DUKES

Protochips, Inc. Morrisville, NC. USA

The development of *in situ* and *operando* techniques, which transform the transmission electron microscope (TEM) into a real-time nanoscale laboratory, has opened exciting windows into dynamic processes that control a material's growth, phase transformation and degradation behaviours. Experiments previously limited to bulk samples on the benchtop, or that required time-consuming, iterative sample preparation, such as temperature cycling, electrical analysis, catalysis, and electrochemistry, can now be performed directly within the TEM to provide a clearer understanding of the underlying nanoscale mechanisms and lead to new discoveries. These studies introduce new challenges in data collection, analysis, and reproducibility (Boyes et al., 2020). *In situ* experiments require careful alignment of parameters from multiple sources as the changing sample conditions, applied stimuli and measured activity must be accurately aligned and indexed to the corresponding TEM images (Damiano et al., 2022).

The Protochips' family of *in situ* systems, Fusion-AX (temperature, electrical and electro-thermal), Poseidon-AX (liquid and electrochemistry), and Atmosphere-AX (gas environments and catalysis) combine unparalleled *in situ* TEM hardware with a machine-vision platform designed to streamline and enhance TEM operation and workflows, consolidate experimental parameters and metadata, and employ machine-assisted algorithms to aid decision making. Here we will present case studies that apply *in situ* techniques to study relevant bulk metallurgical processes such as corrosion (Kovalov et

al., 2022; Schilling et al., 2017; Zhong et al., 2016), and phase transformation during annealing (Shao et al., 2022) and hardening processes (Hillel et al., 2022) at the nanoscale level. Images and metadata generated during an experiment performed using Protochips' *in situ* - AX system is collected and indexed through the machine vision software, AXON. User-triggered changes during the experiment (such as adjustments to beam conditions, detector acquisitions, the *in situ* environment, and applied stimuli) and measured sample responses are organized into an experimental timeline making it easy to sort, filter and analyze large datasets. The robust features and straightforward design of the *in situ* - AX systems coupled with a powerful machine-vision software enables users to take advantage of the latest innovations of *in situ* research and explore the dynamic nanoscale world around them.

## References:

- Boyes, E. D., LaGrow, A. P., Ward, M. R., Martin, T. E., Gai, P. L. Visualizing Single Atom Dynamics in Heterogeneous Catalysis Using Analytical *In Situ* Environmental Scanning Transmission Electron Microscopy. *Philosophical Transactions of the Royal Society A: Mathematical, Physical and Engineering Sciences* 2020, 378 (2186), 20190605. <https://doi.org/10.1098/rsta.2019.0605>.
- Damiano, J., Walden, S., Franks, A., Marusak, K., Larson, B., Coy, M., Nackashi, D. AXON Dose: A Solution for Measuring and Managing Electron Dose in the TEM. *Microsc. Today* 2022, 30 (4), 22–25. <https://doi.org/10.1017/S1551929522000840>.
- Kovalov, D., Taylor, C. D., Heinrich, H., Kelly, R. G. Operando Electrochemical TEM, Ex-Situ SEM and Atomistic Modeling Studies of MnS Dissolution and Its Role in Triggering Pitting Corrosion in 304L Stainless Steel. *Corrosion Science* 2022, 199, 110184. <https://doi.org/10.1016/j.corsci.2022.110184>.
- Schilling, S., Janssen, A., Zaluzec, N. J., Burke, M. G. Practical Aspects of Electrochemical Corrosion Measurements During *In Situ* Analytical Transmission Electron Microscopy (TEM) of Austenitic Stainless Steel in Aqueous Media. *Microsc Microanal* 2017, 23 (4), 741–750. <https://doi.org/10.1017/S1431927617012314>.
- Zhong, X. L., Schilling, S., Zaluzec, N. J., Burke, M. G. Sample Preparation Methodologies for *In Situ* Liquid and Gaseous Cell Analytical Transmission Electron Microscopy of Electropolished Specimens. *Microscopy and Microanalysis* 2016, 22 (6), 1350–1359. <https://doi.org/10.1017/S1431927616011855>.
- Shao, S., Zhu, X., Ten, V., Kim, M. J., Xia, X. Understanding the Impact of Wall Thickness on Thermal Stability of Silver–Gold Nanocages. *J. Phys. Chem. C* 2022, 126, 7337–7345. <https://doi.org/10.1021/acs.jpcc.2c01433>.
- Hillel, G., Kalabukhov, S., Frage, N., Zaretsky, E., Meshi, L. Direct Observation of Initial Stages of Precipitation Hardening Process in Commercial Al 6061 Alloy. *J Mater Sci* 2022, 57 (22), 10395–10406. <https://doi.org/10.1007/s10853-022-07341-2>.

## HIGH SPATIAL RESOLUTION EDS MAPPING USING STEM-SEM. SAM MARKS<sup>1</sup>, SONIKA ROBERTSON<sup>2</sup>

<sup>1</sup>Oxford Instruments NanoAnalysis, High Wycombe HP12 3SE, <sup>2</sup>Oxford Instruments NanoAnalysis, Concord, MA 01742.

Traditional SEM-EDS analyses employ high acceleration voltages with 20 kV being the standard along with longer working distances; this limits the spatial resolution for EDS maps to around 30 to 50 nanometers and any further resolution improvements at those conditions demand considerable effort. Low voltage SEM-EDS analysis combined with a reduced working distance helps minimize the interaction volume and match the high-resolution condition of the SEM. An alternative route to improve the spatial resolution of EDS maps entails using higher accelerating voltage in conjunction with an electron transparent sample with STEM-SEM. Theoretical assessment of X-ray generation for iron K line at a range of acceleration voltages, 2 kV, 30 kV, and 200 kV chosen to represent low kV SEM mode, STEM-SEM mode, and standard TEM acceleration voltage, respectively, indicated that, under identical acquisition settings, the 30 kV STEM-SEM EDS is significantly more efficient than the 200 kV TEM analysis; furthermore, a 200 kV TEM would require almost two to three times the solid angle to attain equivalent X-ray count rates to a 30 kV STEM-SEM

EDS. This laid the foundation for a comparative study assessing the effectiveness of the three aforementioned modes in resolving the  $\gamma'$  and  $\gamma''$  precipitates in a nickel superalloy sample (Fig. 1). The STEM-SEM mode has shown to be extremely effective for analyzing features ranging from 3 nanometers to 100 nanometers whilst warranting considerably less column alignment and enabling faster analyses in comparison with traditional TEM and STEM techniques when multiple samples are to be analyzed. The resolution improvements achieved by the STEM-SEM mode indicate that the technique can not only reduce TEM workload but also, in some cases, provide a strong alternative to traditional TEM and STEM characterization.

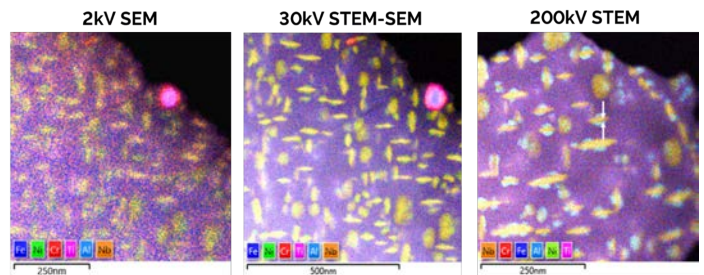
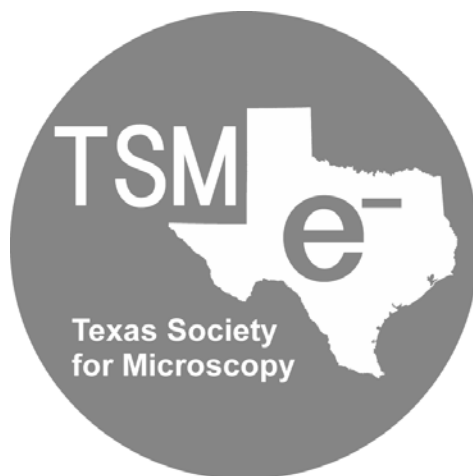


**Figure 1:** Layered element maps collected on a nickel superalloy sample using different image acquisition modes to assess the effectiveness of the different techniques in resolving the ~20-nm precipitates. Left: 2 kV SEM mode; Middle: 30 kV STEM-SEM mode; Right: 200 kV STEM.



# JOIN THE TEXAS SOCIETY FOR MICROSCOPY ON FACEBOOK

<https://www.facebook.com/profile.php?id=100068412613970>



## The 57<sup>th</sup> Texas Society for Microscopy Meeting March 16-17, 2023 Davidson-Gundy Alumni Center at the University of Texas at Dallas, Richardson, TX



VISIT THE TSM WEBSITE  
<https://texas.microscopy.org/>



Advancing Microscopy and Microanalysis



Embracing All Forms of Microscopy

[HOME](#) [ABOUT](#) [MEMBERSHIP](#) [EVENTS](#) [SMALL GRANT](#) [JOURNAL](#) [CONTACT US](#)  

# Welcome to the Texas Society for Microscopy

## About Us

The Texas Society for Microscopy (TSM) was founded in 1963 and has become an informative resource for many scientists since then. We welcome microscopists, researchers, students and administrators from all disciplines and backgrounds who are interested in microscopy or the science of microscopy.

Our non-profit organization is committed to advancing knowledge and understanding of all aspects of microscopy and their applications as they apply to life sciences, materials sciences and industry. We are committed to support students through our **Small Grant Program** and through travel grants to attend our annual meetings. The society is also represented at the meetings of the Microscopy Society of America through our president. The annual meetings of the TSM are a highlight for our members and enjoy wide corporate support.

We invite you to become a member of the TSM and support its mission and vision through your **membership**.

## Upcoming Meetings



2024 TSM Meeting - February 22, 2024 9:00 am

AN AFFILIATE OF THE



AN AFFILIATE OF THE



**VISIT THE TSM WEBSITE**  
<https://texas.microscopy.org/>

## THE TEXAS JOURNAL OF MICROSCOPY IS AVAILABLE ONLINE



Advancing Microscopy and Microanalysis



[HOME](#) [ABOUT](#) [MEMBERSHIP](#) [EVENTS](#) [SMALL GRANT](#) [JOURNAL](#) [CONTACT US](#)  

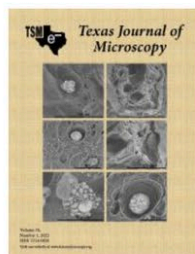
### Texas Journal of Microscopy

The "Texas Journal of Microscopy" is the official journal of the Texas Society for Microscopy (TSM), which is committed to advancing knowledge and understanding of all aspects of microscopy and its application as it applied to life sciences, material sciences and industry. We welcome the submission of scientific papers covering theory, design, methods, application, and practice of microscopy and microanalysis in all fields of life sciences, material sciences, nanotechnology and engineering. Original publications, review articles, and short communications are welcome. Manuscripts will be considered for publication only if they have not been published, or submitted elsewhere, and have passed the peer-review process of suitable reviewers. The "Texas Journal of Microscopy" is an open access journal. Additionally, a print version of the journal is published annually which contains all accepted articles and the abstracts of the annual meeting of the TSM. While non-members will be charged a \$200 processing fee for each published article, publication is free for members of the TSM.

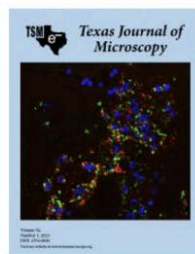
#### Most Recent Issues:



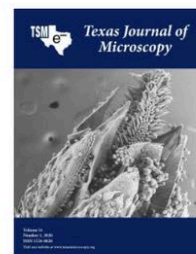
Vol. 54-1



Vol. 53-1



Vol. 52-1



Vol. 51-1 (2020)

#### Archive:

- Volumes 51-59 (2020-2029)
- Volumes 41-50 (2010-2019)
- Volumes 31-40 (2000-2009)
- Volumes 21-30 (1990-1999)
- Volumes 11-20 (1980-1989)
- Volumes 2-10 (1970-1979)
- Volume 1 (1967-1970)

# Corporate Members and Regional Sales Managers



## Andor Instruments, an Oxford Company

andor.oxinst.com/  
860 Aviation Pkwy Ste 1400  
Morrisville, NC 27560  
Phone: 408-850-1139  
Bruno Combettes  
978-402-5023; b.combettes@andor.com  
Ryan Robinson  
978-402-5023; r.robinson@andor.com  
Tomas Silvia Santisteban  
978-402-5023; t.silva@bitplane.com



## Advanced Microscopy Techniques

amtimaging.com  
242 West Cummings Park  
Woburn, MA 01801  
Dominick Camillo  
508-221-4449; dominick@amtimaging.com  
Tom Levesque  
214-883-3194; tlevesque@amtimaging.com  
Adam Maganiello  
508-221-4449; adam@amtimaging.com



## AMETEK, GATAN, EDAX

ametech.com  
85 McKee Dr.  
Mahwah, NJ 07430-2105  
Phone: 201-466-0907  
John Haritos  
201-466-0907; John.haritos@ametech.com  
David Stowe  
David.Stowe@ametech.com



## AVR Optics

avr-optics.com  
187 N Water Street  
Rochester, NY 14604  
Lane Manning  
585-445-7588; lane.manning@avr-optics.com



## BioTek Instruments, Inc. (Now Agilent)

biotek.com  
5301 Stevens Creek Blvd.  
Santa Clara, CA 95051  
David Kurtz  
847-757-3387; kurtzd@biotek.com

Richard Westhoven  
512-2025588; richard.westhoven@agilent.com



## Boeckeler Instruments, Inc.

boeckeler.com  
4650 S. Butterfield Drive  
Tucson, AZ 85714  
Phone: 520-745-0001  
Fax: 520-745-0004  
Peter Strucks  
520-331-2216; peter.strucks@boeckeler.com



## Bruker AXS, Inc.

bruker.com  
3194 Beverly Court  
Murrysville, PA 15668  
Phone: 908-419-8225  
Austin, TX 78747  
John Mastovich  
908-419-8225; john.mastovich@bruker.com  
Stephen Ziegler  
737-262-5004; Stephen.Ziegler@bruker.com



## Discover Echo Inc.

discover-echo.com/  
9530 Padgett St., Suite 101  
San Diego, CA 92126  
Adam Conway  
617-999-2774; aconway@discover-echo.com  
Joanna Harper  
617-999-2774; jharper@discover-echo.com  
Brian Templin  
713-557-8915; btemplin@discover-echo.com



## Electron Microscopy Science/Diatome

emsdiasum.com/microscopy/  
1560 Industry Road, P.O. BOX 550  
Hatfield, PA 19440  
Phone: 800-523-5874  
Fax: 215-412-8450  
Stacie Kirsch  
215-415-8400; Stacie@ems-secure.com  
Robert Armstrong  
215-412-8400; rarmstrong@emsdiasum.com



## Evident

(formerly known as Olympus Scientific Solutions)  
evidentscientific.com/en/  
48 Woerd Ave  
Waltham, MA 02453  
Phone: 781-419-3900  
Eric Bridenbaugh  
780-419-3900; eric.bridenbaugh@evidentscientific.com  
Al Butzer  
701-238-1267; al.butzer@evidentscientific.com



## E.A. Fischione Instruments, Inc.

fischione.com  
9003 Corporate Circle  
Export, PA 15632  
Phone: 724-325-5444  
Nicole Dengler  
724-325-5444; nm\_dengler@fischione.com  
Paulina Koszowska  
724-325-5444; p\_koszowska@Fischione.com



## Hirox USA, Inc.

hirox-usa.com  
100 Commerce Way  
Hackensack, NJ 07601  
Phone: 201-342-2600  
Edvina Bassano  
201-342-2600; edvina@hirox-usa.com  
Cody Driver  
201-342-2600; driver@hirox-usa.com



## Hitachi High Technologies America

hitachi-hta.com  
1375 North 28th Ave.  
PO Box 612208  
Irving TX 75261  
Phone: 214-537-2158  
Fax: 972-615-9300  
Robert Passeri  
847-946-3788; robert.passeri@hitachi-hightech.com  
Matthew Reinoehl  
847-946-3788; matthew.reinoehl@hitachi-hightech.com



## Horiba Scientific

horiba.com/int/scientific/  
20 Knightsbride Rd.

Horiba Scientific cont.

Piscataway, NJ 08854  
Chris John  
415-996-3510; chris.john@horiba.com  
Andrey Krayev  
415-996-3510; andrey.krayev@horiba.com



### IXRF Systems

ixrfsystems.com  
10421 Old Manchaca Rd., Suite 620  
Austin, TX 78748  
Phone: 512-386-6100  
Fax: 512-386-6105  
Bryan De Verse  
512-386-6100; bryand@ixrfsystems.com  
Andrea Surak  
andreas@ixrfsystems.com  
Robert Tisdale  
512-415-6839; robertt@ixrfsystems.com



Solutions for Innovation

### JEOL USA, Inc.

http://www.jeolusa.com  
13810 Paisano Circle  
Austin, TX 78737  
Phone: 978-495-2176  
Joel Paul  
978-979-8071; jpaul@jeol.com  
Carolyn Rogers  
978-536-2308; crogers@jeol.com



### Leica Microsystems, Inc.

http://www.leica-microsystems.com  
7125 Northland Terrace N., Suite 100  
Brooklyn Park, MN 55428  
Phone: 314-374-9361  
Andrew Lawson  
469-785-9992; Andrew.Lawson@leica-microsystems.com



### Marine Reef International

marinereef.com/  
1048 Irvine Avenue, Suite 634  
Newport Beach, CA 92660  
Phone: 949-723-0283  
Linda Dailey  
903-851-5187; lindasdailey@gmail.com



### M.E. Taylor Engineering, Inc.

semsupplies.com  
SEMico Division  
15817 Crabbs Branch Way  
Rockville, MD 20855  
Gene Taylor  
301-975-9798; sales@semicro.org



### Molecular Devices, LLC.

moleculardevices.com/  
3860 North First Street  
San Jose, CA 95134  
Phone: 800-635-5577  
Robert Moody  
469-662-8381; robert.moody@moldev.com  
Mridula Vishwanath  
469-662-8381; mridula.vishwanath@moldev.com



### NCI, Inc.

ncimicro.com/  
7125 Northland Terrace N, Suite 100  
Brooklyn Park, MN 55428  
Phone: 888-559-3312  
Mike Hehr  
314-374-9361; mikeh@ncimicro.com  
Michael May  
405-788-0775; michaelm@ncimicro.com



### Nikon Instruments Inc.

nikoninstruments.com  
1300 Walt Whitman Road  
Melville, NY 11747-3064  
Phone: 972-693-7779  
Jonathan Ekman  
407-595-6542; jonathan.ekman@nikon.com  
Kara Harmatys  
713-301-9932; kara.harmatys@nikon.com  
Anil Shukla  
407-595-6542; anil.shukla@nikon.com  
Renata Tully  
469-381-4669; renata.tully@nikon.com



### Olympus America Inc.

olympus-lifescience.com  
48 Woerd Ave.  
Waltham, MA 02453  
Phone: 512-230-5624  
Brian Cook  
512-230-5624; Brian.Cook@Olympus-ossa.com  
Ashley Divine  
832-243-7982; ashley.divine@olympus.com

Lance Hall  
512-230-5624; Lance.hall@olympus-ossa.com  
Doug Kennedy  
512-230-5634; doug.kennedy@olympus-ossa.com  
Joseph Lake  
469-580-7565; joseph.lake@olympus.com



### Oxford Instruments America, Inc.

oxford-instruments.com  
300 Baker Avenue, Suite 150  
Concord, MA 01742  
Phone: 978-369-9933 x 201  
Michael Hjelmstad  
987-402-5983; michael.hjelmstad@oxinst.com  
Sonika Robertson  
987-402-5983; sonika.robertson@oxinst.com



### Protochips

protochips.com  
3800 Gateway Centre Blvd., Suite 306  
Morrisville, NC 27560  
Phone: 919-377-0898  
Mike Coy  
612-751-4391; mike.coy@protochips.com  
Gabriela Mendoza  
512-230-6762; Gabriela.Mendoza@protochips.com  
Dylan Wood  
612-751-4391; Dylan.Wood@protochips.com



### RAITH America

raith.com/  
300 Jordan Road  
Troy, NY 12180  
Phone: 518-874-3000  
Kevin Burcham  
701-238-1267; kevin.burcham@raithamerica.com  
Joseph Klingfus  
701-238-1267; Joseph.klingfus@raithamerica.com



### Rigaku

rigaku.com  
9009 New Trails Dr.  
The Woodlands, TX 77381  
Phone: 281-362-2300 ext. 122  
Angela Criswell  
281-362-2300; angela.criswell@rigaku.com  
Michelle Goodwin  
281-362-2300; Michelle.Goodwin@rigaku.com  
Michael Holcomb  
281-362-2300; Michael.Holcomb@rigaku.com

Rigaku cont.

Ted Huang  
281-362-2300; ted.huang@rigaku.com  
Meredith Shi  
346-300-2398; meredith.shi@rigaku.com  
Aya Takase  
281-362-2300; Aya.Takase@rigaku.com  
Viral Vaghela  
281-362-2300; viral.vaghela@rigaku.com

### **TED PELLA, INC.**

Microscopy Products for Science and Industry

**Ted Pella, Inc.**  
tedpella.com  
PO Box 462477  
Redding, CA 96049-2477  
Phone: 530-243-2200 or 800-237-3526  
James Long  
530-227-8329; James\_Long@tedpella.com  
David Rollings  
530-243-2200; sales@tedpella.com  
Kathy Stangenberg  
530-243-2200; sales@tedpella.com



**TESCAN USA, Inc**  
tescan-usa.com  
765 Commonwealth Drive, Suite 101  
Warrendale, PA 15086  
Phone: 512-417-8990  
Mike Craig  
724-772-7433; mike.craig@tescan-usa.com  
Arnold Hope  
724-772-7433; hope.arnold@tescan.com



**Texas A&M University,  
School of Medicine**  
**Integrated Microscopy Imaging Laboratory**  
medicine.tamu.edu/imil/index.html  
8447 Riverside Pkwy  
Bryan, TX 77807  
Malea Murphy  
979-436-9037; maleamurphy@tamu.edu  
Andreea Trache  
281-787-6993; trache@tamu.edu

### **TEXAS STATE UNIVERSITY**

**Texas State University  
Shared Research Operations**  
sro.txstate.edu/  
601 University Drive  
San Marcos, TX 78666  
Phone: 512-245-6635  
Casey Smith  
512-213-7909; cs53360@txstate.edu

### **ThermoFisher SCIENTIFIC**

**FEI / Thermo Fisher Scientific**  
thermofisher.com  
fei.com  
Lee Casalena  
732-236-5061; lee.casalena@thermofisher.com  
Jamie Chermak  
971-724-5929; jamie.chermak@thermofisher.com  
K.D. Derr  
619-944-7633; kd.derr@thermofisher.com  
James Lallo  
732-236-5061; james.lallo@thermofisher.com  
Bill Sgammato  
508-479-6623; bill.sgammato@thermofisher.com  
Dan Snyder  
346-423-8193; dan.snyder@thermofisher.com  
Ciceron Yanez  
281-739-7370; ciceron.yanez@thermofisher.com



**Tousimis**  
tousimis.com  
2211 Lewis Avenue  
Rockville, MD 20851  
Phone: 301-881-2450  
Fax: 301-881-5374  
Hyun Park  
301-881-2450; hjpark@tousimis.com



**The University of Texas at Austin  
Texas Materials Institute**  
tmi.utexas.edu  
204 E. Dean Keeton Str.  
Mailstop C2201  
Austin, TX 78712  
Xun Zhan  
216-577-1650; Xun.Zhan@austin.utexas.edu



**ZEISS MICROSCOPY**  
zeiss.com/nts  
One corporation Way  
Peabody, MA 01960  
Phone: 978-826-1500  
Fax: 978-532-5696 Fax  
Laura Grafflin  
214-924-7249; laura.grafflin@zeiss.com  
Philipp Bastians  
914-7471800; philipp.bastians@zeiss.com  
John Donlon  
800-233-2343; john.donlon@zeiss.com



# The Cutting Edge for Fast TEM Sample Preparation



## Multi-Purpose FIB-SEM JIB-PS500i

## Robust Workflow for High Quality TEM Sample Preparation

### *Atomic Resolution STEM and TEM Sample Preparation*

The all-new JIB-PS500i from JEOL delivers fine milling capabilities essential for fast, high quality lamella preparation. This multi-purpose FIB-SEM enables high throughput sample preparation, high resolution STEM-in-SEM imaging, and analytical analysis.

### *Robust Workflow for Large Samples*

Featuring a large specimen chamber with easy-access door and large high-tilt stage, the JIB-PS500i offers a truly flexible workflow. Transfer from the FIB-SEM to the TEM is seamless with TEM-Linkage, JEOL's double-tilt cartridge.

Scan QR Code  
for Details



www.jeolusa.com • salesinfo@jeol.com  
978-535-5900